ORIGINAL ARTICLE

Potential of remote sensing data to support the seismic safety assessment of reinforced concrete buildings affected by slow-moving landslides

Annalisa Mele[1] · Andrea Miano[1] · Diego Di Martire[2,3] · Donato Infante[3] · Massimo Ramondini[3,4] · Andrea Prota[1]

Abstract

Different forms of hazard can affect structures throughout their existence. The occurrence of a seismic event in areas exposed to different risks or already affected by other phenomena is highly likely, especially in countries characterized by high seismicity and equally high hydrogeological risk, as Italy. Nevertheless, the seismic safety assessment of reinforced concrete (RC) structures is commonly carried out considering the seismic action only, generally applied to an analytical model, neglecting the stress–strain state induced by previous ongoing phenomena. The aim of this work is to highlight the importance of the seismic safety assessment in a multi-hazard analysis, cumulating the action coming from two different hazards: landslide and earthquake. An existing RC building, located in an area affected by an intermittent landslide phenomenon with slow kinematics, that may also be subjected to strong earthquakes, is used as case study. The Differential Synthetic Aperture Radar Interferometry (DInSAR) approach is used to monitor the evolution in time of the landslide. DInSAR deformation data are used to detect surface ground movements applied to building foundations. A non-linear static analysis procedure is implemented for the code-based seismic safety assessment, in two different scenarios. The seismic assessment of the case-study building is implemented in a condition of structure deformed only for gravity loads, and, then, in a state of known landslide-induced deformed configuration. A comparison is proposed between the building seismic safety assessment performed in both cases, with or without the consideration of the landslide-induced displacements, showing the importance of a multi-hazard evaluation.

Keywords Multi-hazard assessment · Earthquake · Landslide · Remote sensing · RC building structural assessment

1 Introduction

The seismic safety assessment of reinforced concrete (RC) structures is commonly carried out considering a single hazard source and an analytical model representing the intact structure, neglecting potential previous damage induced by other phenomena. Different forms of hazard can affect structures throughout their existence, generally not occurring simultaneously, but spaced over the years. This is a scenario that may very likely occur, especially in Italy, a country characterized by high hydrogeological risk as well as high seismicity.

Many methodologies and applications regarding the seismic assessment of existing RC buildings can be found in the national and international literature, aiming to investigate the different problematic aspects of this task, such as the choice of the proper modeling strategy and analysis methodology [1–5] and the consideration of the different source of uncertainties in the modeling phase [6–8]. Moreover, different studies evaluate the structural damage in the existing RC structures as consequence of displacements induced by landslides [9–13] or other hazard sources, such as subsidence [14, 15], ground consolidation [16], mining activities [17], excavations [18], and variations in the temperature

✉ Andrea Miano
  andrea.miano@unina.it

1 Department of Structures for Engineering and Architecture, University of Naples Federico II, Naples, Italy

2 Department of Earth, Environment and Resources Sciences, University of Naples Federico II, Naples, Italy

3 SINTEMA Engineering Srl, Spin-Off University of Naples Federico II, Naples, Italy

4 Department of Civil, Architectural and Environmental Engineering, University of Naples Federico II, Naples, Italy

distribution in the structural elements [19], monitored through satellite data for consistent time intervals. In fact, all the mentioned hazard sources induce displacements quite slow in time in the existing buildings, which can be easily monitored through remote sensing techniques. Applications about the seismic assessment procedures for existing RC buildings affected also by other ongoing hazard source-induced displacements, instead, are very few. Pitilakis and Fotopoulou [20, 21] proposed a methodological framework for assessing the vulnerability of typical RC buildings subjected to combined ground shaking and earthquake-induced landslide hazards resulting to the construction of coupled fragility curves. Negulescu et al. [22] developed fragility curves for masonry structures affected by permanent ground displacements and earthquakes.

This work aims to present a procedure to assess the seismic safety condition of RC infilled buildings after cumulating the action coming from the two considered hazards landslide and earthquake. Satellite data, derived from the Differential Synthetic Aperture Radar Interferometry (DInSAR) approach, are used to monitor the development of the landslide-induced displacements in time. The DInSAR technique [23] allows to detect displacements of targets on the ground (buildings, rocks, infrastructures, etc.) with millimeter accuracy, carrying out maps of mean displacement rates and time series of deformations [24–30]. This technique has been proven to be a powerful monitoring tool due to its high spatial and multi-temporal coverage, rapid data acquisition, and reasonable costs.

A RC infilled building, constructed in the 60s in Moio della Civitella, (Campania Region, South of Italy), is the target of this research. The municipality of Moio della Civitella belongs to an area affected by an intermittent landslide phenomenon with slow kinematics, and classified as seismic zone 2, according to the most recent Italian territorial seismic classification [31], meaning that it may also be subject to strong earthquakes. Typical deficiencies of pre-seismic designed structures can be found in the case study building. The remotion of the concrete cover on a consistent sample of structural elements, together with non-destructive tests, have highlighted an insufficient number of stirrups in the nodal regions (low confinement in the areas of potential plastic hinges formation), the use of longitudinal and transverse smooth bars, and poor anchorage details for the reinforcement.

A 3D model of the case study building, including also infills, is created based on the information detected from the available original drawings (kindly provided by local practitioners) and an in situ survey made in December 2020. A simulated design is implemented to complete the knowledge process, and literature references are considered to fill the lack of some information. A modeling approach specifically elaborated for RC members with plain bars [32] is considered for the non-linear behavior of beams and columns. As

regards infills, the model proposed by Panagiotakos and Fardis [33] is used.

The processing of COSMO-SkyMed images for the period 2012–2019 allows to obtain the ground displacements. These data, representing the landslide effect acting regardless of the seismic action, are applied in the model at the ground column bases. Then, the non-linear static analysis procedure, also known as "pushover", is implemented in this work for a code-based seismic safety assessment. The main code reference is the Italian National Code, NTC (2018) [34], but the same checks are also required accordingly to Eurocode 8—Part 3 (EC8-3, [35]). Moreover, pushover analysis is used to calculate the "seismic safety index" (named for brevity "safety index") [36], also called in the literature "seismic safety factor" [37] and defined in NTC (2018) [34] with reference to the Life-Safety (LS) and Damage Limitation (DL) *limit state (ls)*. The assessment of the seismic safety of the building, considered to be in a state of known landslide-induced damage, is conducted. The goal and the novelty of this work are to present a procedure to quantify the changes in the seismic safety of a given structure previously damaged by quasi-static landslide-induced displacements. The methodology is repeatable elsewhere for the seismic assessment of RC buildings. The comparison results between the seismic safety assessment of the building expected in both cases, with or without the consideration of the precedent landslide-induced displacements, show the importance of this multi-hazard evaluation.
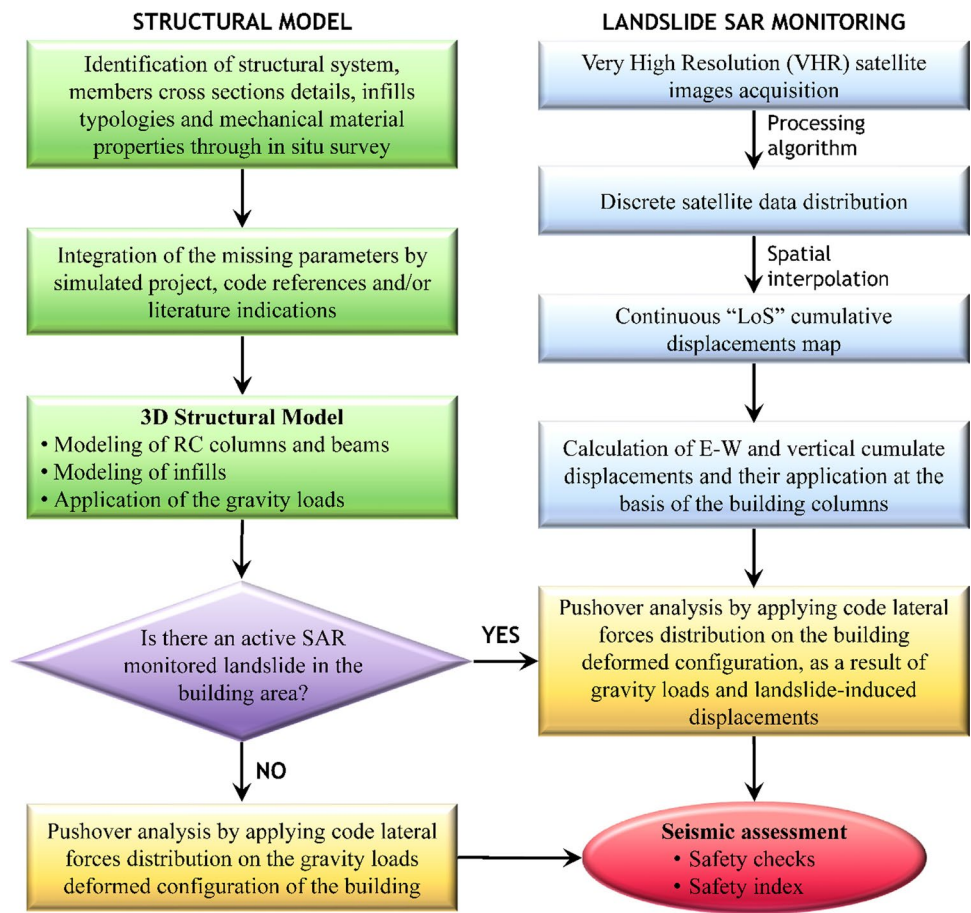
2 Proposed methodology

The DInSAR approach and the seismic assessment procedure followed in this work—including safety checks and safety index assessment—are explained in detail in Sects. 2.1 and 2.2, respectively. In Sect. 3, the case study building and the structural model creation are presented. Then, the DInSAR analysis and the displacement application for the case study building are shown in Sect. 4.1. Moreover, in Sect. 4.2, the building seismic assessment is implemented, both with and without the consideration of the previous landslide-induced displacements, showing a comparison between the results in the two different conditions. In this work, the two considered hazard actions, earthquake [EQ] and landslide [LAN], are considered independent. Then, the effects induced by the two hazards are cumulated. The proposed methodology is schematized in the flowchart presented in Fig. 1.

2.1 DInSAR approach

DInSAR approach is an extremely effective tool for detecting, with millimetric accuracy, deformation phenomena of the Earth's surface. It is based on the use of time series of

Fig. 1 Flowchart of the proposed methodology

STRUCTURAL MODEL

- Identification of structural system, members cross sections details, infills typologies and mechanical material properties through in situ survey
- Integration of the missing parameters by simulated project, code references and/or literature indications
- **3D Structural Model**
  - Modeling of RC columns and beams
  - Modeling of infills
  - Application of the gravity loads
- Is there an active SAR monitored landslide in the building area?
  - **NO**: Pushover analysis by applying code lateral forces distribution on the gravity loads deformed configuration of the building

LANDSLIDE SAR MONITORING

- Very High Resolution (VHR) satellite images acquisition
- *Processing algorithm*
- Discrete satellite data distribution
- *Spatial interpolation*
- Continuous "LoS" cumulative displacements map
- Calculation of E-W and vertical cumulate displacements and their application at the basis of the building columns
- **YES**: Pushover analysis by applying code lateral forces distribution on the building deformed configuration, as a result of gravity loads and landslide-induced displacements

Seismic assessment
- Safety checks
- Safety index

radar images [38], acquired by sensors installed on satellite platforms that travel along semi-polar orbits. Therefore, due to the Earth rotation, and to the fact that SAR sensor is pointed on the same side with respect to the velocity vector in the orbit trajectory, an area can be enlightened from East—during descending orbits (from North to South)—or from West—during ascending ones (from South to North) (Fig. 2).

The angle formed by the perpendicular line to the trajectory orbit (Line of Sight—LoS) and the look line is called "look angle" ("incident angle"). DInSAR approach is based on the maintaining of the same "electromagnetic signature" for the radar targets, namely "Permanent Scatterers" (PSs) [40], in all images, thus preserving information over time even if the acquisition geometry and weather conditions vary. PSs are typically buildings, metallic structures, rocks or in any case elements present on the ground, for which the electromagnetic characteristics do not vary appreciably over time.

Interferometric analyses are based on radar images, which are arrays of pixels, each of which is associated with a resolution cell. An image contains amplitude and phase information. The amplitude identifies the portion of the electromagnetic field incident on all objects belonging to the ground resolution cell and backscattered toward the sensor. The
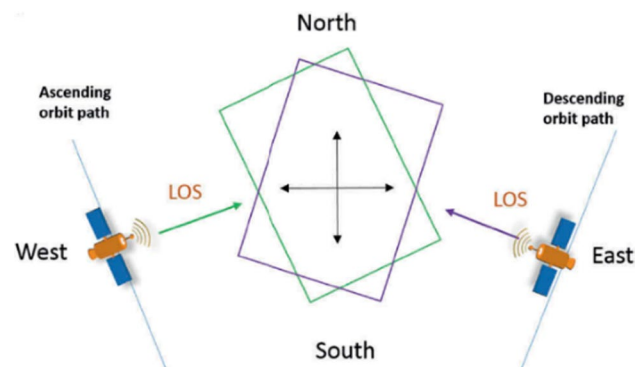

Fig. 2 Ascending and descending SAR acquisition geometries (modified from Vassileva et al. [39])

phase φ (°) is given by the contribution of multiple terms, summarized in the following equation [41]:

$$\varphi = \psi + 4\pi/\lambda \cdot r + \alpha + n, \qquad (1)$$

where ψ (°) is the term due to the reflectivity of the target, α (°) is a contribution related to the atmosphere, r (m) is the displacement induced by movement, λ (m) is the wavelength

of the sensor, and n (°) is the noise of the acquisition system, related to the Earth curvature, the signal-to-noise ratio (SNR) and the instrumental noise. The factor $4\pi/\lambda$ is referred to as the *propagator term*. Through Eq. (1), it is possible to obtain the displacement r induced on the structure by natural phenomena (e.g., landslide as in the case study). In detail, by comparing the phase information of each homologous pixel between two or more SAR images, captured at different times (provided by the same measuring station), it is possible to estimate the displacement along the sensor line of view, by Eq. (1). Therefore, the phase values of radar images contain information on the double sensor-target path taken by the signal and, hence, constitute the basic information for all the interferometric techniques [41]. By comparing a pair of images acquired over the same area, but at two different times, it is possible to analyze the phase variation between the two images through the interferogram, and highlight any differences due to deformation phenomena. Therefore, having a stack of images on the same area, it is possible to obtain maps of PSs characterized by mean displacement rates and time series of deformation, measured along the LoS.

Moreover, if succeeding in combining two acquisitions coming from descending and ascending orbits, it is possible to evaluate the horizontal and vertical components of the displacement vector, to be correlated to the existing phenomenon. This operation can be better understood by considering a x, y, z Cartesian coordinate system, in which the three directions coincide with the horizontal East–West (E–W), North–South (N–S) and vertical, respectively (Fig. 3).

In such reference system, the displacement vector D can be calculated as

$$D = D_x s_x + D_y s_y + D_z s_z, \qquad (2)$$

where D_x, D_y, and D_z are the velocity vector components along the horizontal (E–W and N–S) and vertical directions, and s_x, s_y, and s_z are the unit vectors of the three coordinate axes of the Cartesian system. Thus, using the mean velocity

values D_a and D_d, obtained from the PSs database, the following system is derived:

$$\begin{cases} D_a = D_x s_{xasc} + D_y s_{yasc} + D_z s_{zasc} \\ D_d = D_x s_{xdesc} + D_y s_{ydesc} + D_z s_{zdesc} \end{cases}, \qquad (3)$$

where s_{xasc}, s_{yasc}, s_{zasc}, s_{xdesc}, s_{ydesc}, and s_{zdesc} represent the direction cosines of the respective displacement vectors D_a and D_d. In this system, the number of the unknown variables (D_x, D_y and D_z) is higher than that of the equations, and therefore, it cannot be solved. However, due to the geometrical characteristics of the acquisition, the component on N–S direction appears to be negligible [24], thus allowing to solve the previous system and to assess motion components in E–W and vertical directions (D_h and D_v respectively, corresponding to x and z directions)

$$\begin{cases} D_a = D_v \cos\theta_{asc} + D_h \sin\theta_{asc} \\ D_d = D_v \cos\theta_{desc} + D_h \sin\theta_{desc} \end{cases}. \qquad (4)$$

Finally, to obtain a distributed data, a spatial interpolation is carried out using the Inverse Distance Weighted (IDW) approach, setting a resolution cell of 3 m × 3 m, for each analyzed year of monitoring. This allows to obtain the displacement values referred to the columns of the investigated structure.

Cosmo-SkyMed images have been processed through DInSAR technique to detect landslide-induced deformations. Such images have been obtained by means of an agreement between Department of Earth Science, Environment and Resources of the University of Naples Federico II and Italian Spatial Agency (ASI), in the framework of MapItaly Project [42]. Specifically, in this study, the results obtained in a previous work [13] for the period 2012–2016 (Table 1) have been extended to 2019. In detail, X-band stripmap in ascending and descending mode images, characterized by a ground resolution of 3 × 3 m, acquired in the time span January 2017–March 2019 (Table 1) has been processed using *SUBSIDENCE* software, developed at Remote Sensing

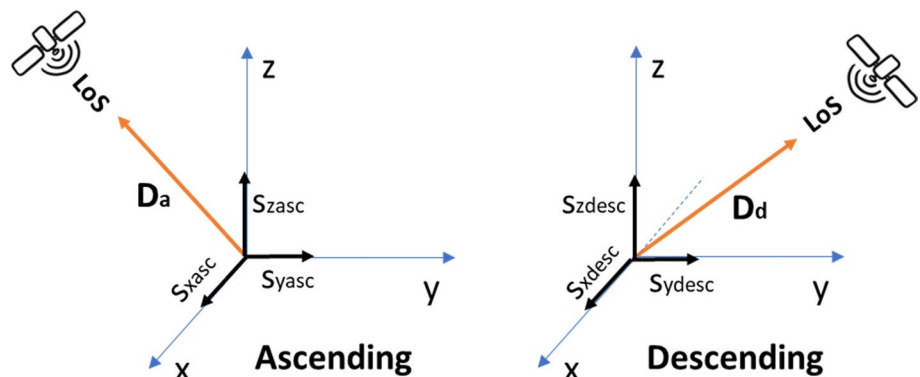**Fig. 3** LoS direction cosines in both ascending and descending geometries

Table 1 SAR data stacks analyzed in this study

Satellite	Orbit	First period (Miano et al. [13])	# Scenes	Second period	# Scenes
Cosmo-SkyMed	Ascending	Jan 2012–Dec 2016	76	Jan 2017–Mar 2019	50
Cosmo-SkyMed	Descending		66		47

Laboratory (RSLab) of the Universitat Politecnica de Catalunya of Barcelona, which implements Coherent Pixels Technique–Temporal Phase Coherence (CPT-TPC) approach [43, 44].

CPT-TPC has been used to obtain ground displacements from satellite radar images. A detailed description of the whole algorithm can be consulted in [43, 44]. The implementation of DInSAR mean displacement rate maps is obtained by seven processing steps: image co-registration, satellite orbit calculation, generation of differential interferograms, targets' selection, evaluation of linear term deformations, assessment of non-linear term rates, and result geocoding from radar coordinates to Universal Traverse Mercator (UTM). Specifically, starting from the ascending and descending datasets, all images have been coregistered. Then, using spatial and temporal baseline thresholds of 100 m and 300 days, respectively, it has been possible to identify 280 interferograms in ascending and 245 interferograms descending orbits. In particular, the first dataset consists of 50 images acquired in ascending geometry with time-revisiting variable between 16 and 76 days in the time span January 2017–March 2019, while the second dataset consists of 47 images acquired in descending geometry with time-revisiting variable between 6 and 96 days for the same time interval. CPT-TPC allows to select points in the investigated area and is characterized by a phase quality higher than a threshold value set by the operator according to the error in the displacement estimation considered acceptable (in this case less than 1.5 mm), which in turn is a function of the expected mean displacement rate. In this case, a phase quality value equal to 0.7 has been set in both geometries to obtain a displacement error lower than 1.5 mm and to select an adequate number of points.

2.2 Seismic assessment procedure

To evaluate the condition of the building, a non-linear static analysis procedure, also known as "pushover", has been implemented. As recommended in NTC (2018) [34], two monotonically increasing patterns of lateral forces are applied to the structure in the control point, represented by the center of the roof floor masses. In the pushover curves of the multi-degree of freedom (MDOF) systems, the base shear, V_b, is expressed as function of the roof displacement, Δ_{top}.

To proceed with the seismic safety checks, it is necessary to find the so-called "inelastic demand point", D_{inel} [45].

Initially, the MDOF pushover curve is divided by the modal participation factor Γ, so obtaining the "capacity curve" of the equivalent single degree of freedom (SDOF) system. The parameters characterizing the SDOF (period T^*, yield strength F_y^*, and ultimate displacement d_u^*) allow to calculate the return period capacity and the peak ground acceleration (PGA) capacity, indicated as $PGA_{capacity}$, for which the failure mechanism is reached. The capacity curve relative to the equivalent SDOF is bilinearized according to [46] and [34]. The resulting curve is characterized by an elastic–plastic behavior. The slope of the elastic branch indicates the stiffness of the equivalent SDOF, k^*. The procedure for the determination of D_{inel} is implemented in the Acceleration Displacement Response Spectrum (ADRS) space, having the spectral displacements on the abscissas, and the spectral accelerations on the ordinates. In the ADRS space, the elastic seismic spectrum is reported, as well as the equivalent bilinear curve adapted by dividing its ordinates by the mass of the SDOF system, m^*. The extension of the elastic branch of the bilinear curve intersects the ADRS spectrum in the elastic demand point, D_{el}, which coordinates represent the acceleration and the displacement required by the elastic SDOF system. Starting from D_{el}, the inelastic demand point, D_{inel}, is determined by following the steps deeply explained in the standard [46]. Once the results of the pushover analysis are obtained, the seismic assessment procedure consists into two different phases: (1) the local seismic safety checks for two limit states, as prescribed in the NTC (2018) [34]; (2) the calculation of a global safety index for the structure, named safety index, ζ_E.

2.2.1 Seismic safety checks

The seismic safety checks are conducted for the LS-*ls* and the DL-*ls*, as prescribed in the NTC (2018) [34] for the structures in Usability Class (CU) II, defined as those constructions which functionality involves normal crowding, such as the case study building. It can be noted that LS-*ls* and DL-*ls* are, respectively, equivalent to the Limit State of Significant Damage (SD) and to the Limit State of Damage Limitation (DL) defined in EC8-3 [35]. The probability of exceedance in the reference period, PVR, is equal to 63% for DL-*ls*, and 10% for LS-*ls* [34].

The structural checks in the inelastic demand point D_{inel} at LS-*ls* are performed with regards to ductile mechanisms and brittle mechanisms. The structural capacity of beams and columns in ductile terms is evaluated according to

the capacity model suggested by the Commentary to NTC (2018) [46], that is the same model adopted in the EC8-3 [35], in terms of chord rotation capacity. For RC members under cyclic loading, the value of the total chord rotation capacity at ultimate, θ_u, for near collapse limit state, is computed as

$$\theta_u = \frac{1}{\gamma_{el}} \cdot 0.016 \cdot 0.3^\nu \cdot \left[\frac{\max(0.01;\omega')}{\max(0.01;\omega)} \cdot f_c \right]^{0.225}$$
$$\cdot \left(\frac{L_v}{h} \right)^{0.35} \cdot 25^{\left(\alpha \cdot \rho_{sx} \cdot \frac{f_{yw}}{f_c} \right)} \cdot \left(1.25^{100 \cdot \rho_d} \right), \tag{5}$$

where γ_{el} is a safety coefficient equal to 1.5 for primary seismic elements; ν is the dimensionless axial effort acting on the whole RC section; ω and ω' are the mechanical percentages of longitudinal reinforcement in tension and compression, respectively; f_c and f_{yw} are the concrete compressive strength (MPa) and the yielding transversal tensile strength (Mpa), respectively; L_v is the ratio between moment and shear at the end section; h is the depth of the cross-section; ρ_{sx} and ρ_d are the geometrical percentage of transversal and diagonal reinforcements, respectively; α is a confinement efficiency factor. The chord rotation capacity corresponding to LS-*ls* is assumed to be 3/4 of the ultimate rotation given in Eq. (5).

The brittle failures for beams, columns, and beam-column joints are checked according to the capacity models suggested by the codes [35] and [46]. The value of the shear strength in cyclical conditions, V_R, is calculated based on three contributions, that are the rate due to the magnitude of the axial force on the element, V_N, the contribution given by the concrete resistant mechanisms, V_C, and the shear resistance offered by the transverse reinforcement, V_W, defined as follows:

$$V_N = \frac{h-x}{2L_v} \min(N; 0.55 A_g f_c) \tag{6}$$

$$V_C = 0.16 \max(0.5; 100 \rho_{tot}) \left[1 - 0.16 \min(5; \frac{L_v}{h}) \right] A_g \sqrt{f_c} \tag{7}$$

$$V_W = \rho_{sx} b_w z f_y, \tag{8}$$

where x is the compression zone depth; N is the compressive axial force; A_g is the cross-section area; f_c is the concrete compressive strength, divided by the partial safety factor; ρ_{tot} is the longitudinal reinforcement ratio; b_w is the width of the rectangular section; z is the length of the internal lever arm. The seismic cyclical action can reduce the shear resistance,

according to the ductility demand on the element. Then, the shear strength is calculated combining Eqs. (6), (7) and (8)

$$V_R = \frac{1}{\gamma_{el}} \left[V_N + k(V_C + V_W) \right]. \tag{9}$$

In Eq. (9), γ_{el} is a safety coefficient equal to 1.5 for primary seismic elements, and k takes into account the cyclic reduction of resistance, defined as follows:

$$k = 1 - 0.05 \min\left(5; \mu_\Delta^{pl} \right), \tag{10}$$

where μ_Δ^{pl} is the plastic part of the ductility demand and is defined as $\mu_\Delta^{pl} = \mu_\Delta - 1$. The term μ_Δ indicates the ductility demand, expressed as the ratio between the maximum rotation θ_m for the considered level of seismic action, and the first plasticity rotation, θ_y. According to [46], when $\mu_\Delta < 2$, the shear strength is the higher of the cyclic shear strength provided by (9) and the shear resistance with transverse reinforcement for non-seismic conditions, evaluated through the variable truss inclination model, as the minimum between the compression-shear and the tension-shear resistance [34, 47]. When $\mu_\Delta > 3$, the extent of the demand for plasticity of the element increases, resulting in a reduction of shear strength; therefore, V_R is evaluated by Eq. (9). For intermediate situations with values of μ_Δ between 2 and 3, a linear interpolation is suggested [34].

For unconfined beam-column joints without stirrups, the principal tensile stress approach for the shear capacity is used, adopting the following expression for the compression resistance [46, 48]:

$$\sigma_{jc} = \frac{N}{2A_j} + \sqrt{ \left(\frac{N}{2A_j} \right)^2 + \left(\frac{V_j}{A_j} \right)^2 } \leq 0.5 f_c (\text{MPa}), \tag{11}$$

and the following expression for the tension resistance

$$\sigma_{jt} = \left| \frac{N}{2A_j} - \sqrt{ \left(\frac{N}{2A_j} \right)^2 + \left(\frac{V_j}{A_j} \right)^2 } \right| \leq 0.3 \sqrt{f_c} (\text{MPa}). \tag{12}$$

In Eqs. (11) and (12), N indicates the axial action in the upper column; V_j is the total shear on the joint; A_j regards the geometry of the joint.

The structural checks at DL-*ls* are performed in terms of stiffness, with regards to the displacements. In this case, for CU II, and having explicitly taken into account the infills in the model, the condition can be considered satisfied when the limit provided by the NTC (2018) [34] for masonry structures is respected. It means that the interstory drift between two following floors, d_r, obtained from the seismic analysis, should be lower than 0.2%.

2.2.2 Safety index

The second phase of the seismic assessment procedure regards the calculation of the safety index, ζ_E, [36], that is a very useful parameter to measure the seismic safety level of a building. All the steps of the procedure to calculate ζ_E are well described in Cosenza et al. [36] and Frascadore et al. [37]. The safety index ζ_E is defined as the ratio between the demand PGA, based on the seismic actions prescribed from the code for the considered *ls*, and the capacity PGA of the building

$$\zeta_E = \left(\frac{\text{PGA}_{\text{capacity}}}{\text{PGA}_{\text{demand}}} \right), \tag{13}$$

where $\text{PGA}_{\text{capacity}}$ and $\text{PGA}_{\text{demand}}$ are, respectively, the PGA corresponding to the first achievement of a failure mechanism in a structural member, and the PGA obtained from the elastic code spectrum for the specific site, both with reference to the considered *ls*.

The $\text{PGA}_{\text{capacity}}$ can be quantified by implementing a procedure in the ADRS space, represented in Fig. 4. Herein, the elastic performance point, C_{el}, can be found starting from C_{inel}, making an inverse process to that made to pass from the D_{el} to D_{inel}. The C_{el} point is characterized by the demand displacement, $S_{d,el}$, inducing failures in the SDOF with elastic behavior. It is located on the extension of the elastic branch of the SDOF capacity bilinear previously described, in the ADRS space, together with the nine elastic demand spectra defined by the Code [34]. The capacity spectrum of the structure is the elastic spectrum that induces failures in the structure. It intercepts the ordinates axes at the $\text{PGA}_{\text{capacity}}$ value. It also intercepts C_{el} space and is univocally defined. The capacity spectrum can be found by interpolating the spectra parameters of the two spectra delimiting the portion of space that contains C_{el}, using the logarithmic form as suggested in [46].
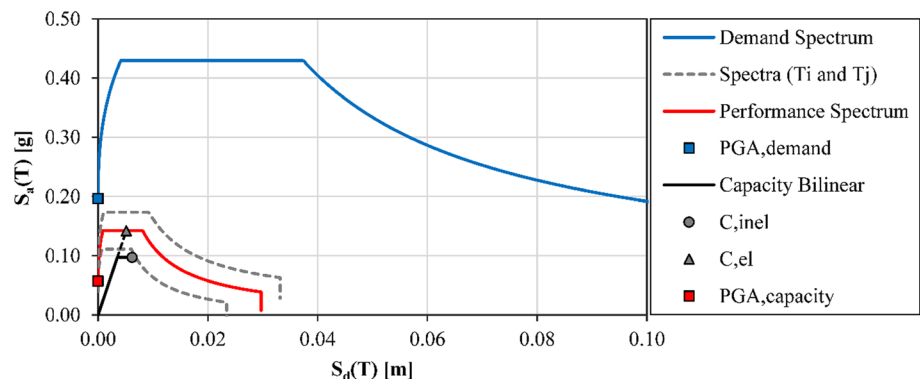
3 Case study and model description

3.1 Landslide phenomena in Moio della Civitella municipality

The methodology presented in this work has been applied to an RC building located in Moio della Civitella (Campania Region, Southern Italy) in the Cilento, Vallo di Diano and Alburni National Park and Geopark. Moio della Civitella is composed of two urban centers: Moio and Pellare (Fig. 5). In the study area, the Crete Nere-Saraceno formation extensively crops out, mainly made up of argillites with intercalated carbonate and silicoclastic arenites, often mantled by weathering-derived sediments. With regards to the geomorphological conditions, Moio della Civitella is characterized by hilly morphologies with low-gradient slopes at altitudes between 600 and 200 m above sea level. In fact, it is widely affected by erosional and gravitational phenomena. According to the Hydro-geomorphological Setting Plan of Hydrographic District of the Southern Apennines (HDSA) [49], slide-flows and roto-translational slides are the most frequent types of slope instability. Specifically, the investigated building falls in the upper part of the landslide (crown area) classified as earth flow. This kind of landslide is characterized by prevailingly horizontal movements, although it is in the crown area. The described intermittent landslide phenomenon with slow kinematics [50–52] induces considerable differential settlements on the foundations of the building.

3.2 Case study building description and in situ surveys

The selected case study is an independent structure, built presumably between 1960 and 1970. Visual surveys allowed to determine accurate dimensions of the rectangular plan, of 11.90 m by 11.95 m, terraces excluded (Fig. 6a–c). It is built on three levels, with a pitched roof which inclination ranges between 15° and 18°. Given the time of construction, and the technical regulations in force at that time [53], it can

Fig. 4 Graphical procedure for the assessment of the safety index in the ADRS space

Fig. 5 Landslide inventory map (2012) and location of the considered building (in the square)
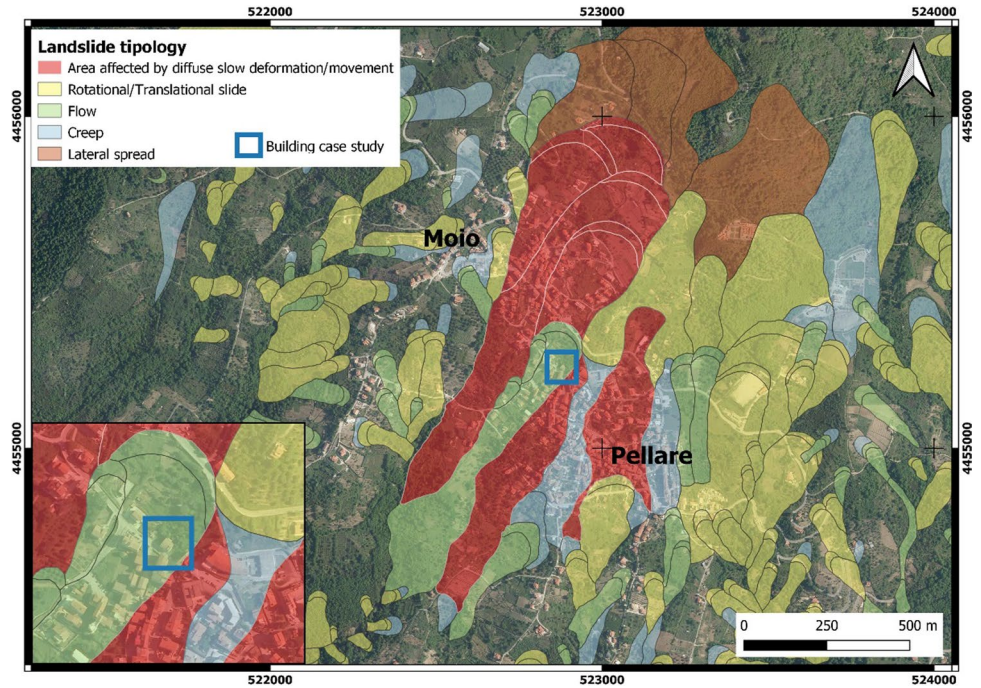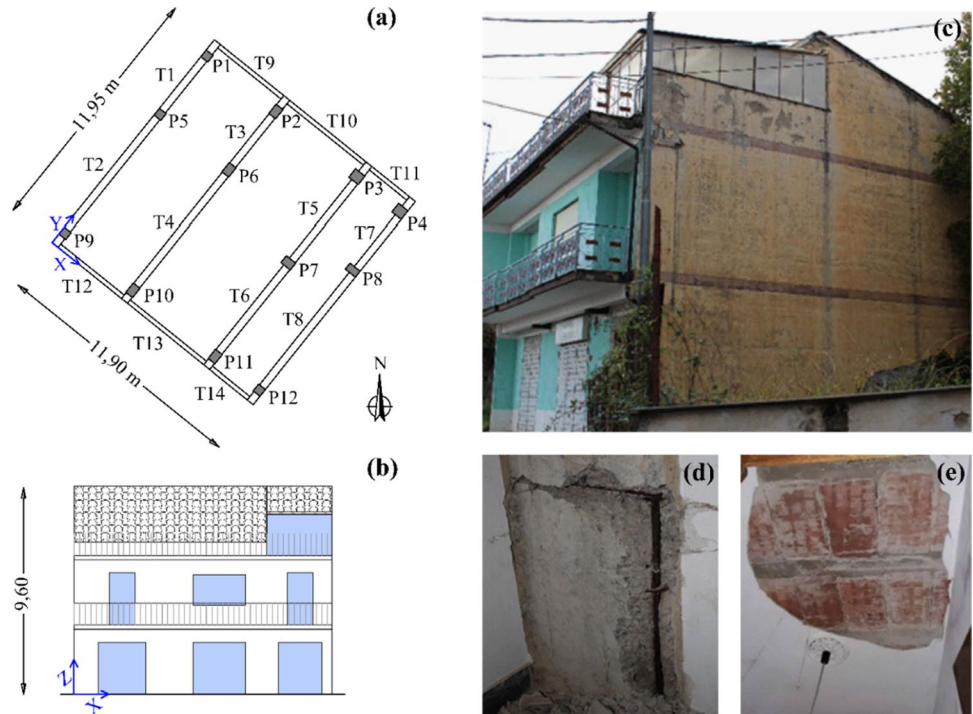

Fig. 6 Geometrical plan (**a**) and front view of the S–W facade (**b**); external picture (**c**); smooth bars at the base of the column (**d**); R.C. with hollow tiles mixed floor, with focus on the RC joists and hollow bricks (**e**) (from in situ survey in December 2020)

be assumed that the building was designed only for gravitational loads, not considering the seismic action.

Authors have been observing the case study since 2010, to enrich the baggage of information regarding the building, mainly through visual inspections and geometrical/ structural surveys. The last visual survey refers to December 2020 (Fig. 6c–e). The visual inspections have led to the

recognition of an RC load-bearing structure with four plane parallel frames, a conventional construction type for a non-seismic structure. From the in situ-inspections, it has been possible to determine the information related to geometrical dimensions and in plane position of beams and columns. The remotion of the concrete cover on a consistent sample of columns, together with non-destructive tests, has allowed

to identify the number and position of longitudinal bars and transversal stirrups. The inspection has highlighted the presence of smooth bars, either for longitudinal or for transversal reinforcements (Fig. 6d).

The dimensions of the rectangular cross sections of the columns are constant over the entire height and are (in cm) 40×55 or 40×40, with exception of the stair columns, which are 55×50, 60×35 and 55×40. The columns are reinforced with 4 longitudinal bars ϕ 16 in the corners of the cross-section, and stirrups ϕ 6/20″. The beams belonging to the structural frames have (in cm) 35×60 rectangular cross sections. Secondary beams, with 20×50 cross sections, orthogonally link the four frames at the ends. The beams reinforcement has been evaluated through a simulated design, following the Italian Standard in force at the construction period [53]. Then, the result of the simulated design has been combined with the typical construction procedures (based on building location and construction age), obtained by interviewing local engineers. Therefore, for the primary beams, 9 bars ϕ 16 in the tensed area and 3 bars ϕ 16 in the compressed area have been adopted. For the secondary beams, instead, 3 bars ϕ 16 in the tensed area and 2 bars ϕ 16 in the compressed area have been adopted. The transversal reinforcement has been quantified in stirrups ϕ 6/15″. Given the structural scheme, all the beam-column joints result to be unconfined, since in each joint, at most, two beams converge.

The missing parameters, related to the mechanical material properties, have been taken from the studies of Verderame et al. 2001 [54] and [55], respectively, for steel and concrete. These works assessed the mechanical properties of steel and concrete in RC structures built in Italy in the 60s. The case study building has also been constructed in the same years. Then, these values are considered to be reliable, being based on a consistent population of structures (232 samples for steel and 490 for concrete), similar to the case study building. In synthesis, it has been assumed that Aq42 smooth steel bars are present, with an average yield strength f_{ym} of 328.6 MPa and an elastic modulus E of 200,000 MPa. Moreover, according to [55], the average value of the concrete characteristic cubic compressive strength has assumed to be as 25.7 MPa. Consequently, applying the appropriate conversion, a cylindric mean compressive strength f_{cm}, of 21.3 MPa, and an elastic modulus, E, of 27,607 MPa have been obtained, based on the expression $E = 22000 \cdot \left(f_{cm}/10 \right)^{0.3}$, provided in [34]. In addition, the visual inspections have allowed to identify the presence of different types of infills in the perimeter walls, shown in the detail in Fig. 7.

In particular, the South-West side presents regular tuff infills with a thickness of 25 cm on the ground floor and on one field of the second floor. The other field of the second floor is realized in solid clay bricks of $12 + 12$ cm. The remaining infills are constituted by a double-leaf vertical hollow clay bricks infill walls with a thickness of $8 + 12$ cm. Mechanical properties of tuff, hollow clay, and solid clay bricks are summarized in Table 2.

For tuff and solid clay bricks, the medium values of the intervals proposed in the Italian Commentary to NTC (2018) [46] have been assumed for the mechanical properties. For hollow clay bricks, they have been derived from Ricci et al. [56], who carried out experimental tests on infill walls

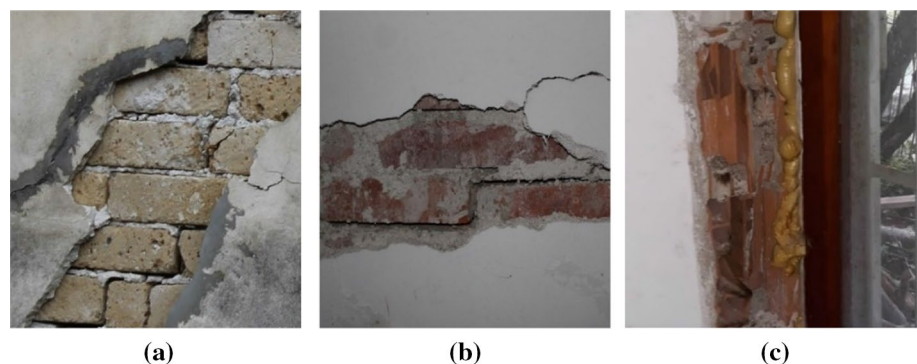**Fig. 7** Infills details: tuff (**a**); solid clay bricks (**b**); hollow clay bricks (**c**)

(a)   (b)   (c)

Table 2 Mean values of infills mechanical properties

Mechanical property	Symbol [unit]	Tuff	Hollow clay bricks	Solid clay bricks
Elastic modulus	E_{mh} [N/mm^2]	1410	1255 (parallel to holes)	1500
Shear modulus	G_{mh} [N/mm^2]	450	315	500
Tensile strength	τ_o [N/mm^2]	0.060	0.215	0.090

constituted by hollow clay bricks with thickness equal to 8 cm. The slight reduction in tension resistance of the 12-cm sized bricks, compared to 8-cm-sized bricks (as highlighted in Di Domenico et al. [57]) has been taken into account through a light correction on the masonry tensile strength τ_o (as already discussed in Miano et al. [13]). Then, also for hollow clay bricks, the mechanical properties values can be considered reliable.

3.3 Modeling description

In this section, the adopted lateral response models for beams, columns, and infills are explained in detail. Moreover, a description of the 3D assembly of the structural model, created using SAP2000 (v. 21.0.2 [58]), is provided.

3.3.1 Modeling of beams and columns

The inelastic cyclic response of RC members has been reproduced by applying a modeling approach specifically elaborated for RC members with plain bars [32]. The nonlinear flexural behavior, represented in Fig. 8a, has been concentrated at the ends of RC elements. Characteristic points/conditions of the base moment (M)—chord rotation (θ) multilinear relationship have been defined as: the yielding point $M_y - \theta_y$, the peak load point $M_{max} - \theta_{max}$, the "*ultimate*" condition point with the attainment of $0.8 M_{max} - \theta_{ult}$, and the zero-resistance point, corresponding to the complete loss of lateral load capacity of the element. For the identification of the above-mentioned characteristic points, by adopting the axial load ratio v and the shear span-to-depth ratio (L_s/d), the mechanical and the geometrical transverse reinforcement ratio (respectively, ω_{sw} and ρ_w), a "fixed-end-rotation coefficient" ($l_{ba}d_b/d\sqrt{f_c}$), and the splice length-to-longitudinal bar diameter ratio (l_0/d_b), the following parameters have been adopted:

The ratio between the effective stiffness, EI_{eff}, and the gross section stiffness, EI_g:

$$EI_{eff}/EI_g = 0.074 \bullet 8.1^v \bullet (1 + 0.30 \bullet L_s/d). \quad (14)$$

The maximum moment M_{max}, predicted attempting that $M_{max}/M_y = 1.14$, with M_y calculated by means of a section fiber analysis.

The corresponding post-yielding plastic chord rotation, θ_{max}^{pl}

$$\theta_{max}^{pl} = 0.0026 \bullet 0.106^v \bullet \left(1 + 1.20 \bullet l_{ba}d_b/d\sqrt{f_c}\right) \\ \bullet \left(0.49 + 0.51 \bullet \min(l_0/d_b)/50\right). \quad (15)$$

The post-capping plastic chord rotation at conventional "ultimate" condition, θ_{ult}^{pc}

$$\theta_{ult}^{pc} = 0.033 \bullet 0.0013^v \bullet \omega_{sw}^{0.51} \bullet \left(l_{ba}d_b/d\sqrt{f_c}\right)^{1.61}. \quad (16)$$

The post-capping plastic chord rotation at the attainment of zero lateral load capacity, θ_0^{pu}

$$\theta_0^{pu} = \min\left(0.0022 \bullet 0.0050^v \bullet 227^{(\rho_w \bullet 100)} \bullet \left(1 + 3.74 \bullet l_{ba}d_b/d\sqrt{f_c}\right); 0.11\right). \quad (17)$$

The softening stiffness toward zero lateral load capacity, K_0

$$K_0 = \max(29 \bullet 407^v \bullet \left(\rho_w \bullet 100^{-1.65}; 700\right). \quad (18)$$

In addition, it has been assumed that $\theta_0^{pu} \leq 4\theta_{ult}^{pc}$ and $K_0 \geq 0.80 M_{max}/\theta_0^{pu}$, to avoid modeling issues.

The predictive equations for "partial" deformability contributions, reported above, are also represented in Fig. 8a. The intersection point can be defined by means of the following equations:

$$\theta_{int} = \frac{K_0\theta_0 - (1 + 0.20\theta_{max}/\theta_{ult}^{pc})M_{max}}{K_0 - 0.20M_{max}/\theta_{ult}^{pc}} \quad (19)$$

Fig. 8 Characteristic points and assumed parameters of the base moment (M)—chord rotation (θ) response envelope (**a**); force–displacement envelope for infills by Panagiotakos and Fardis (1996) (**b**)
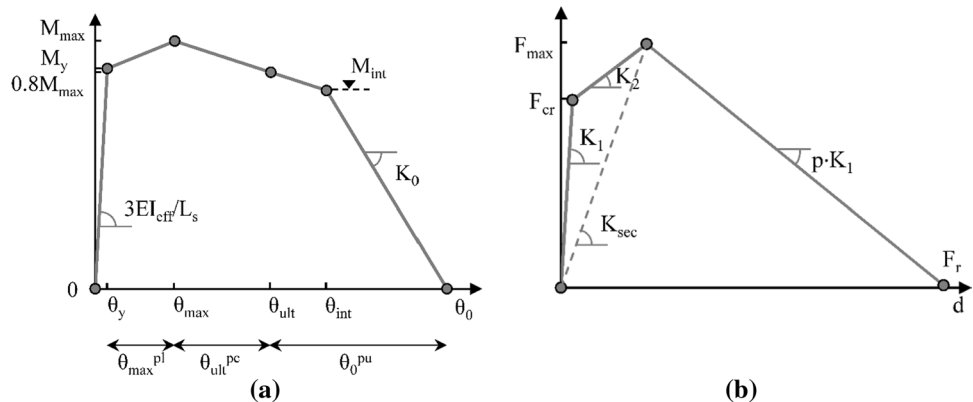
$$M_{\text{int}} = \left(1 - 0.20\frac{\theta_{\text{int}} - \theta_{\text{max}}}{\theta_{\text{ult}}^{pc}}\right)M_{\text{max}}. \tag{20}$$

Equations (14)–(20) are proposed in Di Domenico et al. [32]. The fourth-linear moment-chord rotation bonds have been assigned as flexural plastic hinges at the end cross sections of each element, beam, and column, concentrating the whole plasticity in only such sections.

The shear behavior of RC elements has not been modeled. In fact, based on the existing literature (e.g., [59, 60]), that regards existing RC buildings, the first step of the procedure has been a pre-verification of the expected failure mechanism of the members. The failure mode of members was predetermined by comparing the expected flexural and shear performance (assessed without using safety factors), and, in particular, by comparing the predicted yielding moment, divided by the element shear length, with the predicted shear strength. Then, the elements have been verified with respect to shear mechanism in post-processing, using code-based formulations presented in Sect. 2.2, which are more conservative than performance considerations, due to the introduction of different safety coefficients (on mechanical materials properties and members capacity formulations).

3.3.2 Modeling of the infills

Recent studies [61–63] have highlighted how the presence of infills contributes to the global response of the structure, notably increasing the lateral stiffness of RC buildings. For this reason, each infill panel has been modeled with a couple of equivalent diagonal struts resistant to compression, according to Al-Chaar [64] and Fardis [65]. The infills lateral response has been modeled following the equivalent single strut model proposed by Panagiotakos and Fardis [33]. According to the latter, the initial stiffness (K_1)—up to the diagonal cracking of the infill—and the Mainstone's [66] stiffness secant to peak (K_2) are equal to

$$K_1 = \frac{G_m t_w l}{h} \tag{21}$$

$$K_2 = \frac{E_m a t_w \cos^2 \theta}{D}, \tag{22}$$

where G_w is the masonry shear modulus; l and h are the length and the height of the infill panel, respectively; t_w is the net thickness of the masonry; a and D are the width and the length of the diagonal strut equivalent to the infill panel, respectively.

The softening branch has a slope defined as $p \cdot K_1$, where p has been fixed at -3% for tuff bricks and solid clay bricks (considering an average condition of the valued suggested

by Fardis [67] between -1.5% and -5%), and at -1.6% for hollow clay bricks, following the indications of Ricci et al. [68] and in line with Calvi and Bolognini [69]. The cracking resistance is evaluated as $F_{\text{cr}} = \tau_0 t_w l$; hence, the maximum strength F_{max} is defined by increasing F_{cr} of the 30%. In this study, the backbone ends in correspondence of a lateral strength equal to 1% F_{cr}, neglecting the residual resistance of the panel (Fig. 8b).

The three-linear lateral force–displacement bond has been assigned at the middle cross-section of each diagonal strut as axial hinges. More details about the evaluation of the geometric characteristics can be found in [13].

3.3.3 3D assembly of the structural model in SAP2000

A 3D structural model has been created using SAP2000 (v. 21.0.2 [58]), in which beams and columns have been modeled as horizontal and vertical 2D elements, respectively, while infills have been reproduced as couples of diagonal 2D elements, representing compression-resistant struts. The columns of the first floor have been fixed by restraints at the base to take into account the presence of foundations. The 3D model is shown in Fig. 9. In Fig. 10, the labeling of the building fields is represented (AB, BC, A'B', and B'C' are the fields including infills without openings, while CD, DE, EF, C'D', D'E', and E'F' are the fields including also infills with openings). The infills are differentiated as follows: (1) for color, in hollow clay bricks (blue lines), solid clay bricks (orange lines), and tuff bricks (green lines); (2) for typology of line, in: without openings (continuous lines) and with openings (dashed line). The ones with openings have been considered only as line masses and as line loads on the second-floor beams, because of the significant difference in shape from the panels used in the model proposed by Panagiotakos and Fardis [33]. Instead, the ones in the
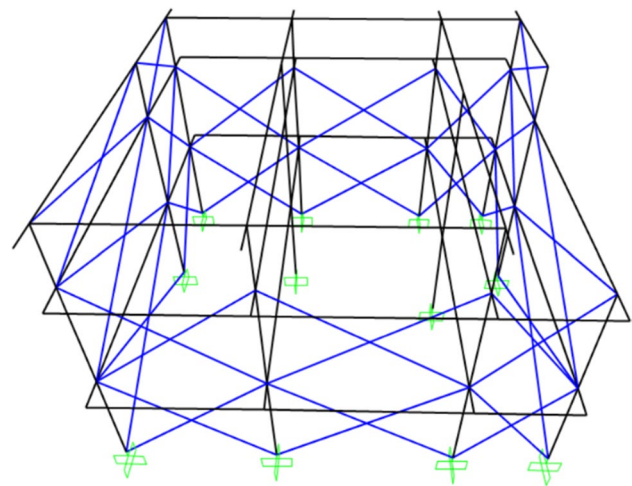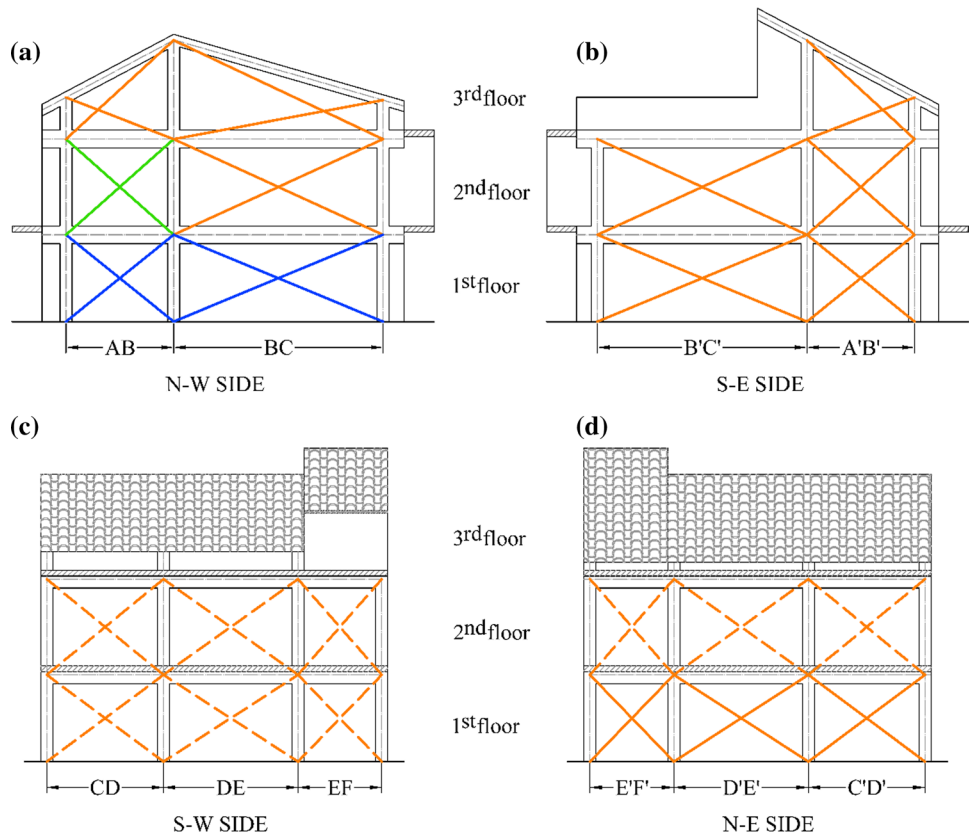

Fig. 9 3D building model

Fig. 10 Building prospects with dentification of the different infills types, differentiated: (i) for color, in hollow clay bricks (blue lines), solid clay bricks (orange lines) and tuff bricks (green lines); (ii) for typology of line, in: without openings [continuous lines (**a**, **b**)] and with openings [dashed line (**c**, **d**)]

fields AB, BC, and A'B' have been modeled, nevertheless being set in frames with beams and columns not mutually orthogonal. Finally, there is a parapet in the B'C' field, and in the EF field, there is no infill because of the presence of a veranda. It is worth noting that in the 3D model, the height of the third level (not uniform in the reality because of the pitched roof) has been set to have an equivalence of areas of the infills between the second- and third-order beams.

The elastic vibration periods of the 3D model, for the first two vibration modes, are, respectively, $T_1 = 0.47$ s and $T_2 = 0.39$ s, in the direction with and without openings, showing a strong reduction with respect to the periods obtained from the structural model without infills modeling.

Pushover analyses in the two directions parallel to the building sides have been carried out by subjecting the structure to a monotonically increasing pattern of lateral forces, as suggested in NTC (2018) [34], once proportional to the fundamental mode of vibration and once proportional to the mass distribution. All the static pushover curves are reported in Sect. 4.2. Herein, a comparison between the pushover curves of the building without and with infills, as example in the case of lateral forces proportional to mass distribution, is reported in Fig. 11, where Δ_{top} is the displacement of the center of gravity of the masses of the roof, and V_b is the total lateral resistance force of the structure.

The comparisons between the pushover curves of the not-infilled (dashed lines) and infilled (continuous lines) model show that the lateral resistance significantly increases in the second case. In particular, the base shear V_b increases until a maximum value and then decreases, related to the softening branch of the infills' and RC elements' backbones. It can be observed that, in the X direction—completely infilled with hollow clay bricks—the increment of lateral resistance is greater with respect to the Y direction—having infills in hollow clay bricks, tuff, and solid clay bricks, as described in Sect. 3.2. The hollow clay bricks, in fact, have a greater resistance with respect to tuff and solid clay bricks. In Fig. 11, the curves have been cut at a value of Δ_{top} approximatively equal to 1% of the height of the building, but it is worth noting that the more Δ_{top} increases, the more V_b of the infilled pushover approaches to the not-infilled building curve. A validation of the structural model with the empirical damages observed in 2015 has been in depth discussed in Miano et al. [13]. In summary, damage empirical observations and analytical previsions, obtained by applying displacements evaluated with the DInSAR approach to the structural model (in the period 2012–2016), agreed that the most damaged facade was the N–W one (see Fig. 6a), showing mainly the typical diagonal tension infill damage.
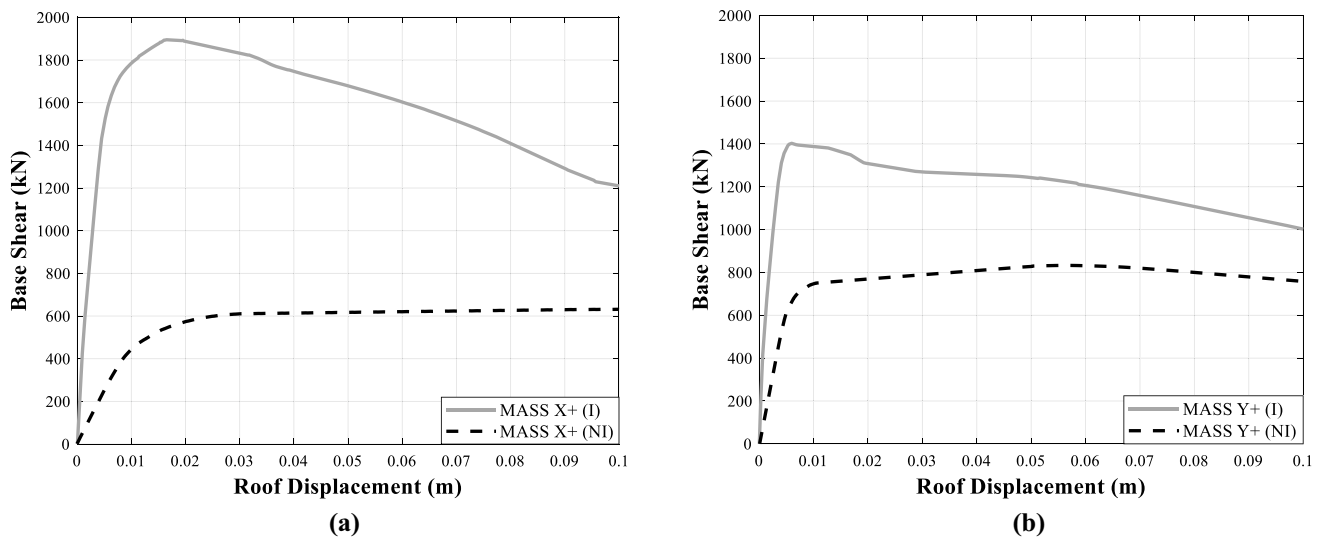
Fig. 11 Comparison of static pushover curves of infilled (I) and not-infilled (NI) building: for X direction (**a**) and for Y direction (**b**)

4 Seismic assessment of the case study building affected by slow-moving landslides

The seismic assessment procedure is initially implemented in a condition of integer structure, deformed only for gravity loads, to verify the seismic safety level of the RC structure ([EQ] scenario). Later, the action of the earthquake is applied to the slow-moving landslide-induced deformed configuration of the building (landslide plus earthquake [LAN + EQ] scenario) and the seismic assessment is replicated.

4.1 DInSAR analysis and displacement application for the case study building

The interferometric results are related to the two investigated periods, respectively, 2012–2016 and 2017–2019. It is possible to highlight that both the inhabited areas of Moio (northern sector) and Pellare (southern sector) are characterized by significant displacement rates along the LoS. In particular, for the period 2012–2016 (Fig. 12), the highest rates have been recorded in the hamlet of Pellare, with values of about 0.75 cm/year, while in the hamlet of Moio, the maximum rates recorded are about 0.40 cm/year. Moreover, for the period 2017–2019 (Fig. 13), the highest rates have been found in the hamlet of Pellare (about 0.60 cm/year), although slightly lower than those recorded previously, confirming the state of activity of the phenomena. Figures 12 and 13 show in detail the PSs identified on the investigated building. As an example, the time series of displacements of two PSs are reported (Fig. 14), respectively, in ascending (A1) and in descending (D1) orbits. The two time series of displacement

assume opposite sign, meaning that the real displacement has a prevalent horizontal component.

Subsequently, the combination of the maps obtained along the two tracks has allowed to detect the cumulated vertical and horizontal E–W components of movement, with millimeter accuracy, at the end of each year of the period 2012–2018, and for the first 3 months of 2019, providing profiles of cumulated vertical and E–W displacements occurred to building foundations. The cumulated vertical and horizontal E–W components of movement at the end of 2019 and 2020 have been obtained by extending the linear regression of the data calculated between 01/2012 and 03/2019 to the end of the mentioned years, for each column. The cumulate displacement profiles are shown in Fig. 15. These displacement values are applied at support at the bases of the first-floor columns. It is to note that the landslide-induced displacements before 2012 have been neglected in the further analysis. This assumption has been also discussed in Miano et al. [13]. However, the goal of this work is to present a novel methodology to combine the effects from landslide and earthquake. Clearly, in a real application, this assumption is not always applicable, and then, it should be carefully checked.

4.2 EQ and LAN + EQ results and comparisons

4.2.1 Seismic safety checks

As described in Sect. 2.2, the first part of the seismic assessment procedure consists in the seismic verifications for the capacity of the RC elements at the LS-*ls*, and for the deformability at the DL-*ls*. The seismic action on the building has been evaluated based on a reference

Fig. 12 Mean velocity maps for the time span 2012–2016 in ascending (**a**) and descending (**b**) orbits; the reference point (black star) and the case study building (black oval) are indicated
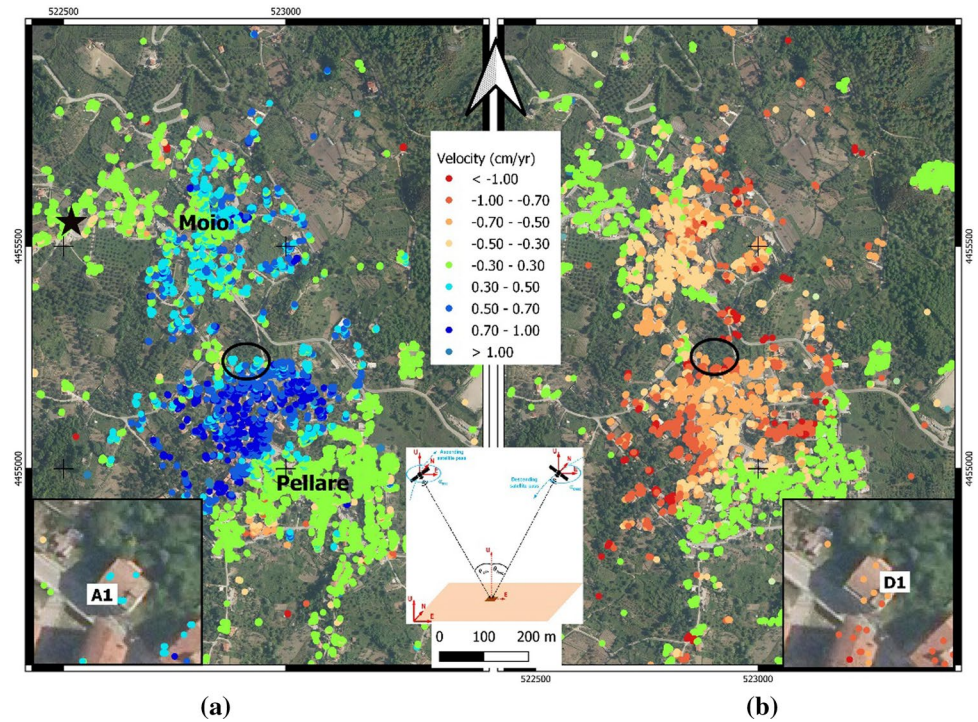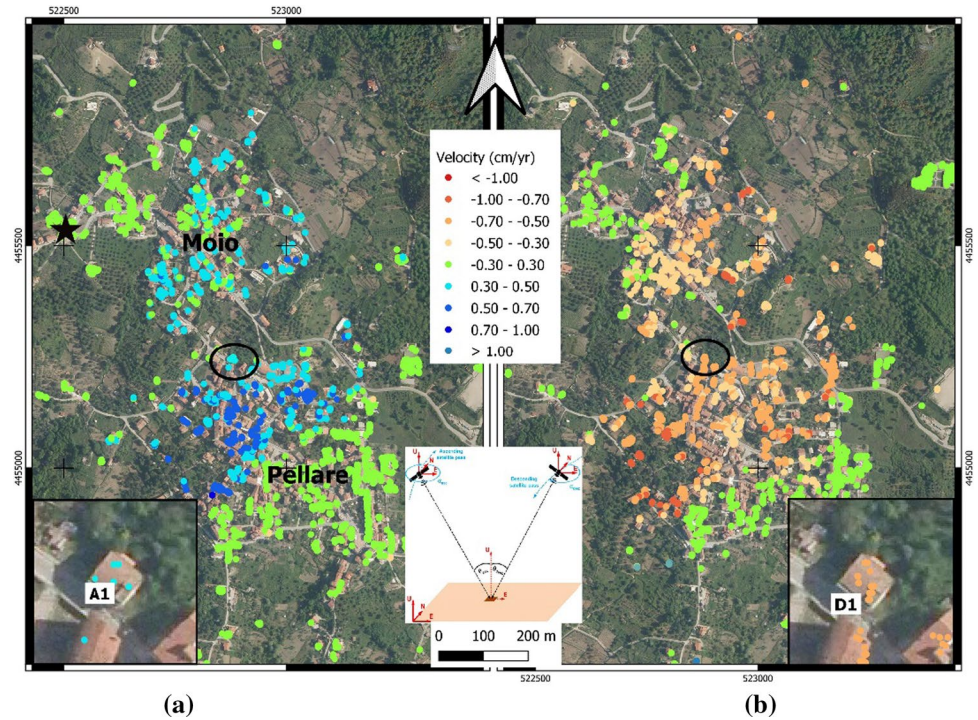
(a)   **(b)**

Fig. 13 Mean velocity maps for the time span 2017–2019 in ascending (**a**) and descending (**b**) orbits; the reference point (black star) and the case study building (black oval) are indicated

(a)   **(b)**

period, V_R, obtained multiplying the nominal life of the structure, V_N (defined as the number of years in which it is expected to maintain specific performance levels) by the coefficient of use, C_U. V_N is fixed at 50 years for constructions with ordinary performance levels, while C_U is equal to 1 for ordinary residential buildings. The horizontal components of the seismic action have been considered through the elastic response spectra in acceleration, appropriately scaled according to the characteristics of the ground. For site effects of sediment soil, based on the outcome of a geological study, category C (Tab. 3.2.II [34]) has been assumed, referred to medium-sized deposits

Fig. 14 Time series of displacements of an ascending (A1) and a descending (D1) PS, located on the investigated building
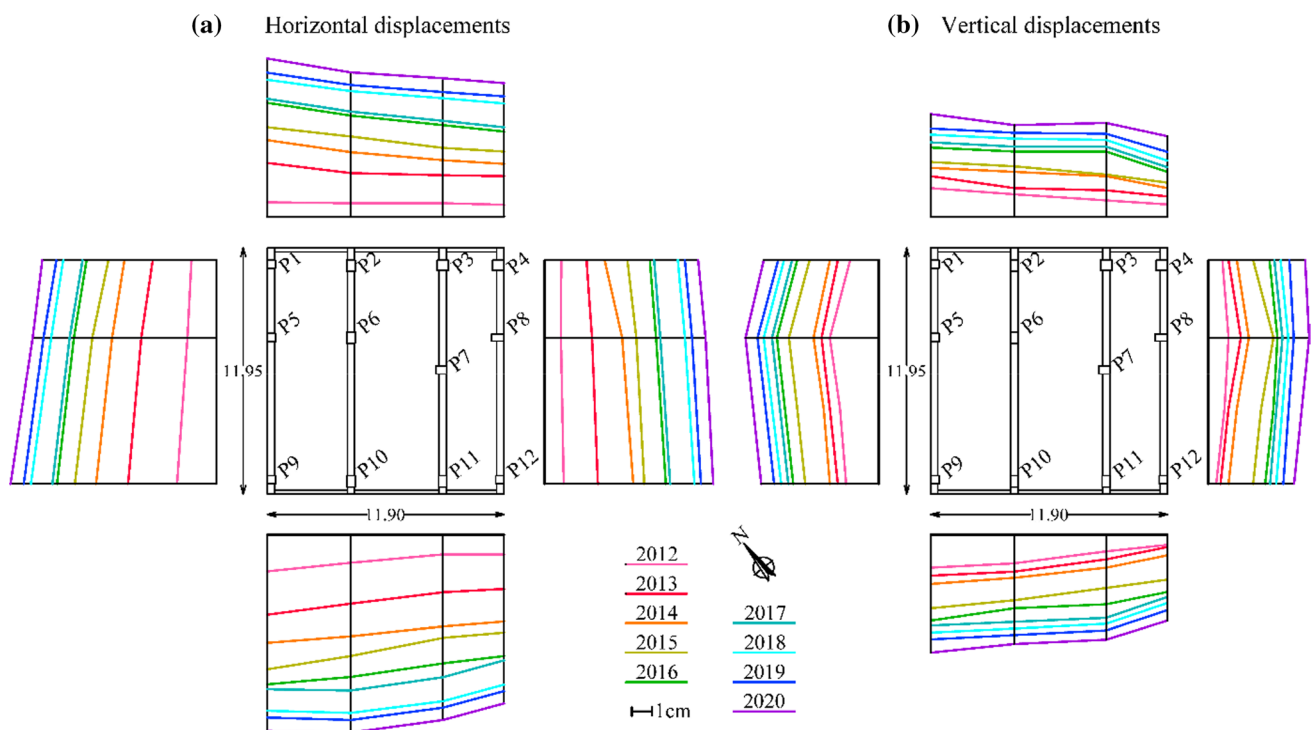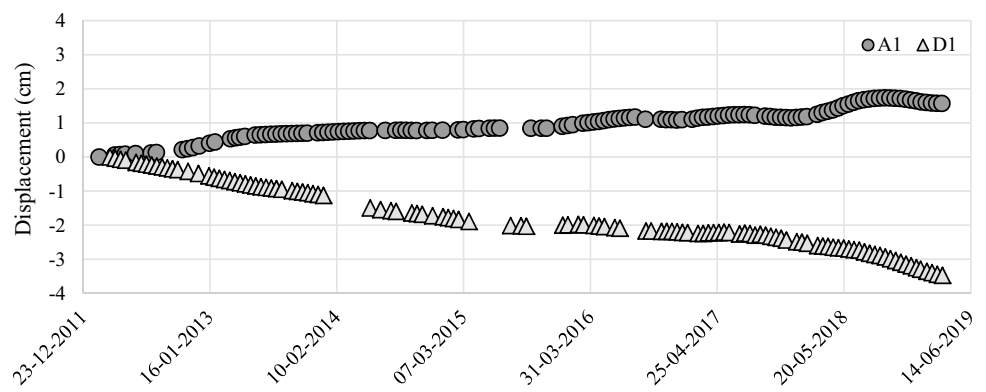

Fig. 15 Displacement profiles extracted for the building foundations at the end of each year in the period 2012–2020

of fine-grained land. Moreover, a T1 category has been assumed for the topographical surface (Tab. 3.2.III [34]).

The EQ scenario provides the seismic assessment of the case-study building implemented in a condition of structure deformed only for gravity loads before the application of the seismic action. In the LAN + EQ scenario, in a first step, the pattern of differential displacements described in Sect. 4.1, that are the landslide-induced cumulative horizontal and vertical displacement components evaluated in the period 2012–2020, has been applied to the structural model. The landslide action causes the onset of a stress/strain state in the structural elements, which become the starting point for the successive application of the seismic action. Then, the seismic assessment procedure has been implemented on the structural deformed condition due not only to gravity loads, but also to the differential displacements induced by the slow-moving landslide affecting the case study building.

As mentioned in Sect. 2.2, non-linear static analyses have been carried out through a step-by-step procedure, by subjecting the structure to two monotonically increasing pattern of lateral forces, applied at the centers of floor mass in the model, one proportional to the fundamental mode of vibration (Mode X and Mode Y), one proportional to the mass distribution (Mass X and Mass Y), where X and Y directions are assumed accordingly to Fig. 6a. Once the results of the pushover analyses have been obtained, the seismic verifications in terms of ductile and fragile mechanisms in the step corresponding to the

inelastic demand point D_{inel}, for the LS-*ls*, and in terms of displacement, for the DL-*ls*, have been carried out.

The pushover curves are represented in Fig. 16, with gray continuous lines for EQ scenario and black dashed lines for LAN + EQ scenario. It can be noted that, in the LAN + EQ scenario, the curves in the X (Fig. 16a, b) and Y (Fig. 16c, d) direction are translated with respect to the axes origin of a displacement quantity in the control point. This is as consequence of the displacements applied at the base of the columns in the model, which cause translations and rotations in the structural elements, leading to an initial displacement in the control point. In each step, the starting imposed displacement component affecting the roof control point, induced by the existing landslide, is summed with the roof displacement induced by the seismic action.

In Fig. 16, the evolutions of the failure sequences found at the two *ls* for both scenarios are compared. The step of the analysis at which the first structural element experiences a failure mechanism has been found and remarked on the related pushover curve. In particular, for LS-*ls*, the tensile-shear failures in beam-column unconfined joints are represented with red triangles, while brittle shear failures, in beams and columns, are indicated with orange squares and yellow circles, respectively. For DL-*ls*, the limit step is marked with a cyan inverted triangle.

The evidence of the structural checks, up to the inelastic demand point D_{inel} at LS-*ls*, for the EQ scenario (indicated with a green pentagram in Fig. 16), has shown that ductile failures are never attained, while tensile–shear failure in beam-column unconfined joints and shear failure mechanisms in beams and columns are expected. In fact, in each
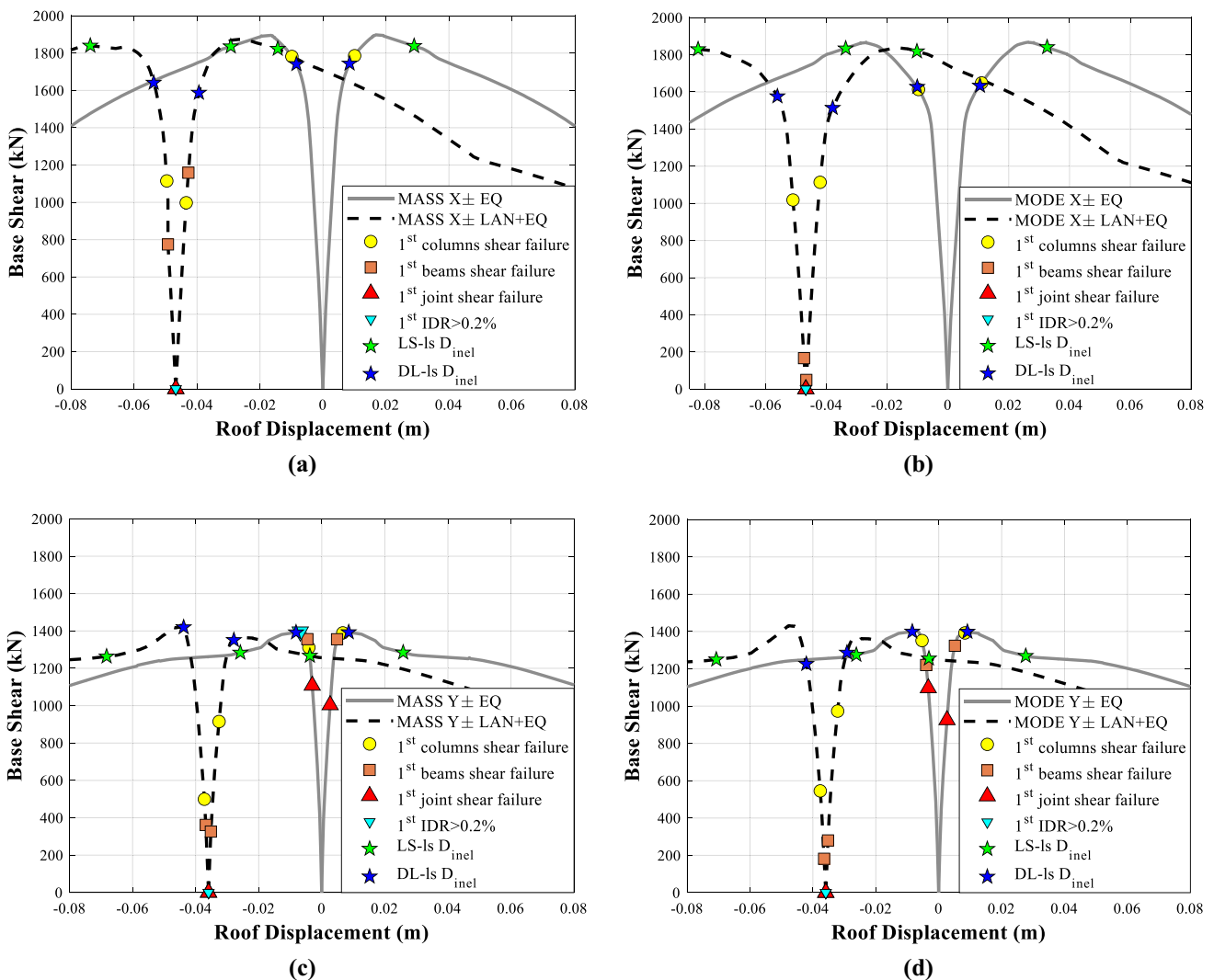

Fig. 16 Comparison of the pushover curves and relative failure mechanism progress of structural elements, until the demand point, in the EQ and LAN + EQ scenarios: mass X (**a**), mode X (**b**), mass Y (**c**), and mode Y (**d**)
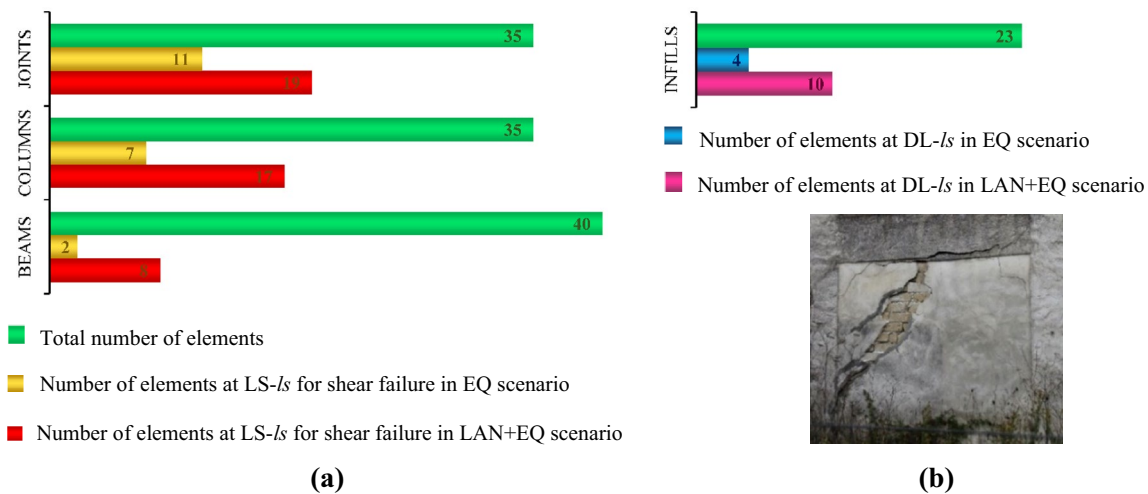
Fig. 17 Number of elements in crisis at LS-*ls* and at DL-*ls*, versus number of total elements, in EQ and LAN + EQ scenarios, with focus on the most damaged infill in 2020 survey

load case, the first ductile failure occurs after the pushover step corresponding to D_{inel}. Then, the ductile failures are never achieved at LS-*ls*. The numerical analyses have also shown that the first failure mechanism attained in the structure is the tensile–shear failure in beam-column unconfined joints.

The seismic verifications for LS-*ls*, repeated for the LAN + EQ scenario, have highlighted that the differential displacements applied at the base of the structural model cause an aggravation of the stress state in the structural elements, that experience failures for lower steps with respect to those attained in the EQ scenario. Moreover, the number of elements in crisis at the LS-*ls*, up to D_{inel}, increases. The results of the non-linear static analysis, performed in the LAN + EQ scenario, have shown that the first elements in crisis are still the joints, for the tensile–shear mechanism, actually at the step zero of the pushover. It means that the action of the landslide causes the failures before the application of the seismic action. The following failure mechanisms attained in the whole structure are beams and columns shear failures. The effect of the landslide does not cause ductile crises in the structure, until the pushover step corresponding to D_{inel}. Then, in the LAN + EQ scenario, such as in the previous EQ scenario, at LS-*ls*, only brittle failures in the structural elements are expected.

As regards the DL-*ls*, the corresponding D_{inel} is indicated with a blue pentagram in Fig. 16. In both the scenarios, it has been searched the first step of each analysis in which the limit of 0.2% for the interstory drift ratio, IDR, was attained (marked on the curves in Fig. 16 with a cyan inverted triangle). The first failure at the DL-*ls* is related to the first floor infills in every case. For LAN + EQ scenario, it can be observed that the infill located in the AB first-floor field (see

Fig. 10) in each case attains the DL-*ls* threshold at the step zero of the pushover. Then, the DL-*ls* is exceeded due to the landslide action. This result is in line with the in situ observation made by the authors during the experienced visual surveys. In fact, the mentioned infill is currently damaged, as can be seen in Fig. 17b.

The investigation of the analysis step, at which the first failure is attained, is a fundamental phase of the seismic assessment, because it characterizes the capacity of the whole structural system for the considered *ls*. Once identified this performance point, the $PGA_{capacity}$ and the safety index can be estimated, as explained in Sect. 2.2.

An overview of the number of the failures at LS-*ls* and at DL-*ls* thresholds, in the corresponding demand points, is reported in Fig. 17. In particular, for LS-*ls*, the number of columns and beams experiencing shear failures (see Eq. 9), as well as the number of joints showing tensile–shear failures (see Eq. 12) are reported. For DL-*ls*, the number of infills for which the maximum IDR exceeds the *ls* threshold is presented. The summary also constitutes a comparison between the seismic assessments performed in the two scenarios.

It can be observed that, from EQ scenario to LAN + EQ scenario, the number of elements experiencing brittle failures at LS-*ls* passes from 11 to 19 for joints, from 7 to 17 for columns, and from 2 to 8 for beams. Moreover, the number of infills attaining DL-*ls* passes from 4 to 10. This increase of the number of elements exceeding the *ls* can be attributed to the action of the landslide, which is active independently from the earthquake.

Before evaluating the safety indexes, a specific comparison on the seismic part of the pushover curves in the EQ and LAN + EQ scenarios is provided in Fig. 18. The

displacements at step zero (related to gravity loads for EQ scenario and to gravity loads and landslide for EQ + LAN scenario) have been eliminated to have a direct comparison on the seismic part of the curves. In Fig. 18, the EQ and LAN + EQ curves are represented in continuous and dashed lines, respectively.

The presented overlapping highlights slight differences between the curves, with a general trend of reduction in terms of maximum strength and initial stiffness for the EQ + LAN scenario. Nevertheless, despite the similarity in the seismic trends, it has been previously demonstrated that the landslide-induced displacements highly affect the results. This is in agreement with the previous considerations about the first elements failures, in some cases occurring even at the step zero of the analysis, and the number of elements in crisis in correspondence of D_{inel}.

4.2.2 Safety index

An overall comparison of the global structural condition between the two scenarios has been carried out in terms of safety index, using the performance point to calculate the minimum anchoring peak ground acceleration determining building failure mechanism, $PGA_{capacity}$, and the safety index ζ_E, as described in Sect. 2.2. The results in terms of safety indexes are reported in Fig. 19 for both scenarios.

It can be observed that the safety index at LS-ls, $\zeta_{E,LS-ls}$ always assumes values less than unity, meaning that PGA_{demand} exceeds $PGA_{capacity}$ in each case of the pushover analysis. In particular, in the EQ scenario, where the effects of the seismic action are evaluated in relation to the only gravity loads deformed building, the final $\zeta_{E,LS-ls}$ is equal

to 0.27 (the minimum ζ_E among the eight values). In the LAN + EQ scenario, taking into account also the existing condition of the deformed building affected by landslide phenomena, $\zeta_{E,LS-ls}$ is equal to 0.11. The structure is not able to withstand the seismic action from which, according to the code, could be invested, but only the 27%, in the EQ scenario, and the 11%, in the LAN + EQ scenario. As noticed in Fig. 16, the first step of the analysis in which a failure is attained at LS-ls is always the step zero; nevertheless, according to *Sisma-Bonus* Guidelines [71], as a lower limit for the determination of $PGA_{capacity}$, the spectrum referred to the Beginning of Damage ls has been considered, corresponding to a seismic event whose return period is conventionally assumed equal to 10 years.

As regards the safety index at DL-ls, $\zeta_{E,DL-ls}$, in EQ scenario, it assumes values very close to unity for each analysis, while in the LAN + EQ scenario, the occurrence of the landslide drastically lowers the $\zeta_{E,DL-ls}$. In this case, the first failures at DL-ls occur at step zero, so $\zeta_{E,DL-ls}$ assumes a unique value of 0.27, corresponding to a spectrum with a return period equal to 10 years.

The illustrated comparison remarks that by neglecting the effects of the existing differential displacements landslide-induced, the safety index obtained for the structure can be overestimated. Other considerations can be done according to the indications of NTC (2018) [34], defining the safety index as the parameter to be compared before and after a seismic upgrading/retrofit process to evaluate the efficacy of the interventions. In detail, for Class II constructions, the value of ζ_E, as a result of a seismic upgrading, should be increased by at least 0.10 at LS-ls, while the seismic retrofit of the building is reached if a ζ_E of at least 0.80 or 1.00 (based on the specific case study condition, [34]) is obtained
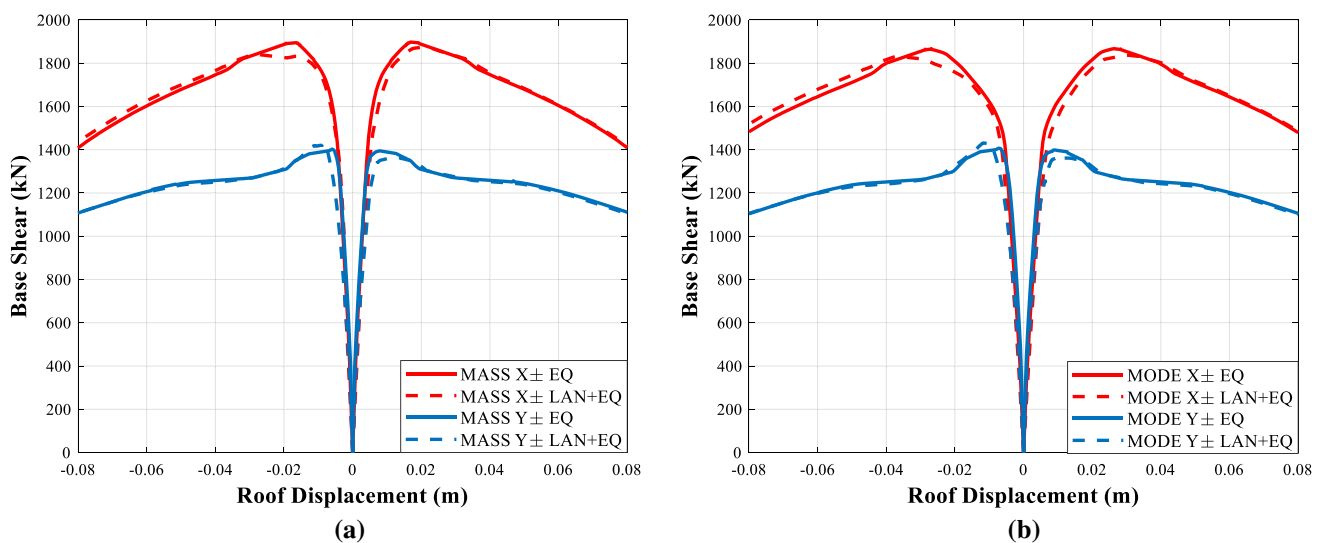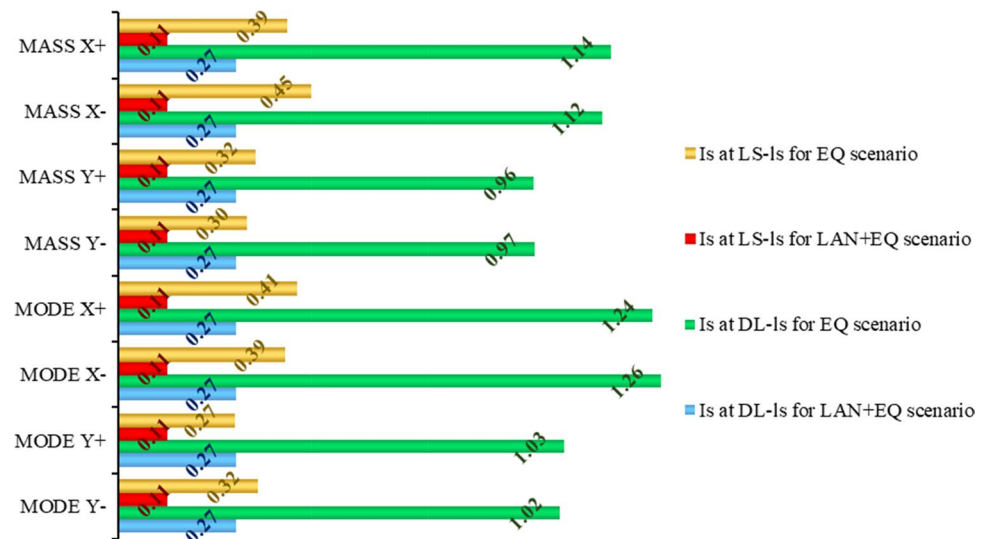

Fig. 18 Comparison of the pushover curves in the EQ and LAN + EQ scenarios: mass X ± and mass Y ± (**a**), mode X ± and mode Y ± (**b**)

Fig. 19 Comparison of the structural safety index in the EQ and LAN+EQ scenarios, at LS-*ls* and at DL-*ls*, for the eight performed analysis

from the analysis at LS-*ls*. Then, the differences in terms of ζ_E between the two scenarios EQ and EQ+LAN have a significant influence on seismic upgrading/retrofit strategies and relative costs. Clearly, many methodologies and applications that analyze in detail the seismic retrofit strategies for existing RC buildings can be found in the literature [3, 72–77]

5 Discussion and conclusions

This study presented the seismic safety assessment of an existing RC infilled building, carried out twice: in a traditional scenario and in a multi-hazard scenario, explicitly considering the effect of the slow landslide-induced movements affecting the structure. The latter displacements have been obtained from the DInSAR technique, employed with reference to the single building scale. A 3D structural model, including infills, has been created, based on the information available from the original geometrical drawings and a detailed survey, obtaining the missing parameters from a simulated design or literature. The landslide phenomenon, which analytically results in differential displacements applied at the base of the building columns in the model, causes a heterogeneous stress–strain path in the structural elements, which becomes the starting condition for the application of the following seismic action.

The seismic safety checks at LS-*ls* have highlighted, both for EQ and for LAN+EQ scenarios, that only brittle failures in the structural elements are expected. In particular:

- The first failure mechanism attained in the structure is the tensile-shear failure in beam-column unconfined joints, then, shear failure mechanisms in beams and columns are expected;

- Ductile failures are never attained;
- In the LAN+EQ scenario, the elements fail for lower steps of the analysis, and the number of elements in crisis at the LS-*ls*, up to D_{inel}, increases, with respect to the EQ scenario;
- The tensile–shear failures of the joints happen at the step zero of the pushover, namely they are induced just by the action of the landslide.

At the DL-*ls*, indeed, the first failure is always related to the first floor infills.

An overall comparison of the global structural condition between the two scenarios has been provided in terms of safety index. The results are herein resumed: (1) the safety index at LS-*ls* assumes values less than unity in both scenarios, meaning that the structure is not able to withstand the code design seismic action, but its value in the LAN+EQ scenario is smaller with respect to that one in the EQ one; (2) the safety index at DL-*ls* assumes values very close to unit in EQ scenario, while drastically lowers in the LAN+EQ scenario.

It is evident that the differential displacements cause an aggravation of the stress–strain state in the structural elements. Then, in the building seismic assessment, the neglect of a pre-existing stress–strain condition leads to an overestimation of the actual residual seismic capacity, represented in a value by the safety index, and consequently to a potential underestimation in the definition of the interventions needed to increase the seismic safety.

The proposed assessment procedure in a multi-hazard analysis can be easily repeated elsewhere to quantify the effect of the active landslide on the seismic assessment of the RC buildings. It is to note that the main aim of the work is not the specific quantification of the effect of the active landslide on the seismic assessment of the RC case study

building, but to show the importance of this multi-hazard evaluation. The seismic assessment can be more or less refined as function of the quantity of information taken from the in situ campaign. Moreover, the methodology presented in this work could furnish useful indications in a forecasting perspective, i.e., in support to the civil protection prevention plans. For phenomena linearly evolving in time, as slow-moving landslides, a prevision of the future displacements for a small number of years could be done, if the trend of the displacements at the structure's base is known. These displacements could be used to carry out an application analogous to that presented in this study, to evaluate the seismic safety margin of the structure, affected by the landslide, in a certain number of years.

Data availability Some or all data, models, or code that support the findings of this study are available from the corresponding author upon reasonable request.

Declarations

Conflict of interest The authors declare that they have no conflict of interest.

References

1. Liel AB, Haselton CB, Deierlein GG. Seismic collapse safety of reinforced concrete buildings II: Comparative assessment of nonductile and ductile moment frames. J Struct Eng. 2011;137(4):492–502. https://doi.org/10.1061/(ASCE)ST.1943-541X.0000275.

2. Fragiadakis M, Vamvatsikos D, Aschheim M. Application of nonlinear static procedures for seismic assessment of regular RC moment frame buildings. Earthq Spectra. 2013;30(2):767–94. https://doi.org/10.1193/111511EQS281M.

3. Miano A, Sezen H, Jalayer F, Prota A. Performance-based assessment methodology for retrofit of buildings. J Struct Eng. 2019;145(12):04019144. https://doi.org/10.1061/(ASCE)ST.1943-541X.0002419.

4. Luo X, Cheng J, Xiang P, et al. Seismic behavior of corroded reinforced concrete column joints under low-cyclic repeated loading. Arch Civ Mech Eng. 2020;20:40. https://doi.org/10.1007/s43452-020-00043-z.

5. Jiao C, Liu Y, Wei B, et al. Seismic performance of circular reinforced concrete columns subjected to compression, bending and torsion with low and moderate shear span ratio. Arch Civ Mech Eng. 2021;21:135. https://doi.org/10.1007/s43452-021-00282-8.

6. Vamvatsikos D, Fragiadakis M. Incremental dynamic analysis for estimating seismic performance sensitivity and uncertainty. Earthq Eng Struct Dyn. 2010;39(2):141–63. https://doi.org/10.1002/eqe.935.

7. Miano A, Jalayer F, Prota A. Considering structural modeling uncertainties using Bayesian cloud analysis. In: 6th ECCOMAS thematic conference on computational methods in structural dynamics and earthquake engineering (COMPDYN 2017), Rhodes Island, Greece, June 15–17, 2017.

8. Jalayer F, Ebrahimian H. Seismic reliability assessment and the nonergodicity in the modelling parameter uncertainties. Earthq Eng Struct Dyn. 2020;49(5):434–57. https://doi.org/10.1002/eqe.3247.

9. Peduto D, Pisciotta G, Nicodemo G, Arena L, Ferlisi S, Gullà G, Reale D. A procedure for the analysis of building vulnerability to slow-moving landslides. In: 1st IMEKO International Workshop on Metrology for Geotechnics, Benevento, Italy, March 17–18, 2016.

10. Infante D, Confuorto P, Di Martire D, Ramondini M, Calcaterra D. Use of DInSAR data for multi-level vulnerability assessment of urban settings affected by slow-moving and intermittent landslides. Proc Eng. 2016;158:470–5. https://doi.org/10.1016/j.proeng.2016.08.474.

11. Infante D, Di Martire D, Confuorto P, Tessitore S, Tòmas R, Calcaterra D, Ramondini M. Assessment of building behavior in slow-moving landslide-affected areas through DInSAR data and structural analysis. Eng Struct. 2019;199:638. https://doi.org/10.1016/j.engstruct.2019.109638.

12. Del Soldato M, Solari L, Poggi F, Raspini F, Tomás R, Fanti R, Casagli N. Landslide-induced damage probability estimation coupling InSAR and field survey data by fragility curves. Remote Sens. 2019;11(12):1486. https://doi.org/10.3390/rs11121486.

13. Miano A, Mele A, Calcaterra D, Di Martire D, Infante D, Prota A, Ramondini M. The use of satellite data to support the structural health monitoring in areas affected by slow-moving landslides: a potential application to reinforced concrete buildings. Struct Health Monit. 2021. https://doi.org/10.1177/1475921720983232.

14. Arangio S, Calò F, Di Mauro M, Bonano M, Marsella M, Manunta M. An application of the SBAS-DInSAR technique for the assessment of structural damage in the city of Rome. Struct Infrastruct Eng. 2014;10(11):1469–83. https://doi.org/10.1080/15732479.2013.833949.

15. Di Carlo F, Miano A, Giannetti I, Mele A, Bonano M, Lanari R, Meda A, Prota A. On the integration of multi-temporal synthetic aperture radar interferometry products and historical surveys data for buildings structural monitoring. J Civ Struct Health Monit. https://doi.org/10.1007/s13349-021-00518-4.

16. Drougkas A, Verstrynge E, Van Balen K, Shimoni M, Croonenborghs T, Hayen R, Declercq PY. Country-scale InSAR monitoring for settlement and uplift damage calculation in architectural heritage structures. *Struct Health Monit* 1475921720942120, 2020. https://doi.org/10.1177/1475921720942120.

17. Herrera G, Tomás R, Vicente F, Lopez-Sanchez JM, Mallorquí JJ, Mulas J. Mapping ground movements in open pit mining areas using differential SAR interferometry. Int J Rock Mech Min Sci. 2010;47(7):1114–25. https://doi.org/10.1016/j.ijrmms.2010.07.006.

18. Giannico C, Ferretti A, Alberti S, Jurina L, Ricci M, Sciotti A. Application of satellite radar interferometry for structural damage assessment and monitoring LifeCycle and Sustainability of Civil Infrastructure Systems. In: 3rd International Symposium on Life-Cycle Civil Engineering (IALCCE '12), Vienna, Austria, October 3–6, 2012.

19. Cavalagli N, Kita A, Falco S, Trillo F, Costantini M, Ubertini F. Satellite radar interferometry and in-situ measurements for static monitoring of historical monuments: The case of Gubbio Italy. Remote Sens Environ. 2019;235: 111452. https://doi.org/10.1016/j.rse.2019.111453.

20. Pitilakis KD, Fotopoulou SD. Vulnerability assessment of buildings exposed to co-seismic permanent slope displacements. XVI ECSMGE Geotechnical Engineering for Infrastructure and Development Edimburgh, September 13–17, 151–174, 2015.

21. Fotopoulou SD, Pitilakis KD. Vulnerability assessment of reinforced concrete buildings at precarious slopes subjected to combined ground shaking and earthquake induced landslide. Soil Dyn Earthq Eng. 2017;93:84–98. https://doi.org/10.1016/j.soildyn.2016.12.007.

22. Negulescu C, Ulrich T, Baills A, Seyedi DM. Fragility curves for masonry structures submitted to permanent ground displacements and earthquakes. Nat Hazards. 2014;74(3):1461–74. https://doi.org/10.1007/s11069-014-1253-x.

23. Gabriel AK, Goldstein RM, Zebker HA. Mapping small elevation changes over large areas: differential interferometry. J Geophys Res. 1989;94:9183–91. https://doi.org/10.1029/JB094iB07p09183.

24. Colesanti C, Wasowski J. Investigating landslides with space-borne synthetic aperture radar (SAR) interferometry. Eng Geol. 2006;88:173–99. https://doi.org/10.1016/j.enggeo.2006.09.013.

25. Costantini M, Ferretti A, Minati F, Falco S, Trillo F, Colombo D, Costabile S. Analysis of surface deformations over the whole Italian territory by interferometric processing of ERS, Envisat and COSMO-SkyMed radar data. Remote Sens Environ. 2017;202:250–75. https://doi.org/10.1016/j.rse.2017.07.017.

26. Ezquerro P, Del Soldato M, Solari L, Tomás R, Raspini F, Ceccatelli M, Fenandez-Merodo JA, Casagli N, Herrera G, G. Vulnerability assessment of buildings due to land subsidence using InSAR data in the ancient historical city of Pistoia (Italy). Sensors. 2020;20(10):2749. https://doi.org/10.3390/s20102749.

27. Crosetto M, Monserrat O, Cuevas-González M, Devanthéry N, Crippa B. Persistent scatterer interferometry: a review. ISPRS J Photogramm Remote Sens. 2016;115:78–89. https://doi.org/10.1016/j.isprsjprs.2015.10.011.

28. Even M, Schulz K. InSAR deformation analysis with distributed scatterers: a review complemented by new advances. Remote Sens. 2018;10(5):744. https://doi.org/10.3390/rs10050744.

29. Solari L, Del Soldato M, Raspini F, Barra A, Bianchini S, Confuorto P, Crosetto M. Review of satellite interferometry for landslide detection in Italy. Remote Sens. 2020;12(8):1351. https://doi.org/10.3390/rs12081351.

30. Talledo DA, Miano A, Bonano M, Di Carlo F, Lanari R, Manunta M, Stella A. Satellite radar interferometry: potential and limitations for structural assessment and monitoring. J Build Eng. 2022;46:103756. https://doi.org/10.1016/j.jobe.2021.103756.

31. Ordinanza del Presidente del Consiglio dei Ministri n. 3274 del 20 marzo 2003, Gazzetta Ufficiale n. 105, 8 maggio 2003 (in Italian).

32. Di Domenico M, Ricci P, Verderame GM. Empirical calibration of hysteretic parameters for modelling the seismic response of reinforced concrete columns with plain bars. Eng Struct. 2021;112:120. https://doi.org/10.1016/j.engstruct.2021.112120.

33. Panagiotakos TB, Fardis MN. Seismic response of infilled RC frames structures. In: 11th world conference on earthquake engineering, Acapulco, México, June 23–28, 1996.

34. DM 17/01/18 (2018) Norme tecniche per le costruzioni, Ministerial Decree (in Italian).

35. Eurocode 8, EN1998-3, Design of structures for earthquake resistance, Part 3: Assessment and retrofitting of buildings, CEN, Brussels, 2005.

36. Cosenza E, Del Vecchio C, Di Ludovico M, Dolce M, Moroni C, Prota A, Renzi E. The Italian guidelines for seismic risk classification of constructions: technical principles and validation. Bull Earthq Eng. 2018;16(12):5905–35. https://doi.org/10.1007/s10518-018-0431-8.

37. Frascadore R, Di Ludovico M, Prota A, Verderame GM, Manfredi G, Dolce M, Cosenza E. Local strengthening of reinforced concrete structures as a strategy for seismic risk mitigation at regional scale. Earthq Spectra. 2015;31(2):1083–102. https://doi.org/10.1193/122912EQS361M.

38. Franceschetti G, Migliaccio M, Riccio D, Schirinzi G. SARAS: a synthetic aperture radar (SAR) raw signal simulator. IEEE Trans Geosci Remote Sens. 1992;30(1):110–23. https://doi.org/10.1109/36.124221.

39. Vassileva M, Giulio Tonolo F, Riccardi P, Lecci D, Boccardo P, Chiesa G. Satellite SAR interferometric techniques in support to emergency mapping. Eur J Rem Sens. 2017;50(1):464–77. https://doi.org/10.1080/22797254.2017.1360155.

40. Ferretti A, Prati C, Rocca F. Permanent scatterers in SAR interferometry. IEEE Trans Geosci Remote Sens. 2001;39(1):8–20. https://doi.org/10.1109/36.898661.

41. Blanco P. SAR Differential Interferometry for deformation monitoring under a multi-frequency approach, 2009 (PhD Thesis).

42. Sacco P, Battagliere ML, Daraio MG, Coletta A. The COSMO-SkyMed constellation monitoring of the Italian territory: the Map Italy project. In: 66th International Astronautical Congress (IAC 2015), Jerusalem, Istrael, October 12–16, 2015.

43. Mora O, Mallorquí JJ, Broquetas A. Linear and non-linear terrain deformation maps from a reduced set of interferometric SAR images. IEEE Trans Geosci Remote Sens. 2003;41:2243–53.

44. Iglesias R, Mallorqui JJ, Monells D, Lopez-Martinez C, Fabregas X, Aguasca A, Gili JA, Corominas J. PSI deformation map retrieval by means of temporal sublook coherence on reduced sets of SAR images. Remote Sens. 2015;7:530–63. https://doi.org/10.3390/rs70100530.

45. Fajfar P. Capacity spectrum method based on inelastic demand spectra. Earthq Eng Struct Dyn. 1999;28(9):979–93. https://doi.org/10.1002/(SICI)1096-9845(199909)28:9%3c979::AID-EQE850%3e3.0.CO;2-1.

46. Circolare n. 7 C.S.LL.PP. 21 gennaio 2019 (2019), Commentary to NTC 2018 (in Italian).

47. Eurocode 2, EN 1992-1-1, Design of concrete structures, Part 1–1: General rules and rules for buildings, CEN, Brussels, 2004.

48. Eurocode 8, EN 1998–1, Design of structures for earthquake resistance, Part 1: General rules, seismic actions and rules for buildings, CEN, Brussels, 2003.

49. Hydro-geomorphological Setting Plan of South Campania River Basin Authority, Via De Gasperi 28, 80133, Naples, Italy, 2012.

50. Calò F, Calcaterr D, Iodice A, Parise M, Ramondini M. Assessing the activity of a large landslide in southern Italy by ground-monitoring and SAR interferometric techniques. Int J Remote Sens. 2012;33(11):3512–30. https://doi.org/10.1080/01431161.2011.630331.

51. Di Martire D, Ramondini M, Calcaterra D. Integrated monitoring network for the hazard assessment of slowmoving landslides at Moio della Civitella (Italy). Rendiconti Online Società Geologica Italiana. 2015;35:109–12.

52. Infante D, Confuorto P, Di Martire D, et al. L'utilizzo di dati DInSAR per la valutazione delle conseguenze indotte sugli edifici da

frane intermittenti a cinematica lenta. XXVI Convegno Nazionale Di Geotecnica. Rome, Italy, June 20–22, 2017 (in Italian).

53. Regio Decreto Legge (R.D.L.) 16 novembre 1939 n°2229 (Suppl. Ord. alla Gazz. Uff. del 18 aprile 1940 n°92) Norme per l'esecuzione delle opere in conglomerato cementizio semplice od armato, 1939 (in Italian).

54. Verderame GM, Stella A, Cosenza E (2001) Le proprietà meccaniche degli acciai impiegati nelle strutture in ca realizzate negli anni'60. X Convegno nazionale "L'Ingegneria Sismica in Italia", Potenza-Matera, 9–13, 2001 (in italian).

55. Verderame GM, Manfredi G, Frunzio G (2001) Le proprietà meccaniche dei calcestruzzi impiegati nelle strutture in cemento armato realizzate negli '60. X Convegno nazionale "L'Ingegneria Sismica in Italia", Potenza, Matera, September 9–13, 2001 (in Italian)

56. Ricci P, Di Domenico M, Verderame GM. Experimental assessment of the in-plane/out-of-plane interaction in unreinforced masonry infill walls. Eng Struct. 2018;173:960–78. https://doi.org/10.1016/j.engstruct.2018.07.033.

57. Di Domenico M, Ricci P, Verderame GM. Experimental assessment of the out-of-plane strength of URM infill walls with different slenderness and boundary conditions. Bull Earthq Eng. 2019;17:3959–93. https://doi.org/10.1007/s10518-019-00604-5.

58. SAP2000 v21.0.2 (2019) Computers and Strucrures, Inc.

59. Setzler EJ, Sezen H. Model for the lateral behavior of reinforced concrete columns including shear deformations. Earthq Spectra. 2008;24(2):493–511. https://doi.org/10.1193/1.2932078.

60. Ricci P, Manfredi V, Noto F, Terrenzi M, De Risi MT, Di Domenico M, Spacone E (2019) RINTC-e: towards seismic risk assessment of existing residential reinforced concrete buildings in Italy. In: Proceedings of the 7th ECCOMAS thematic conference on computational methods in structural dynamics and earthquake engineering, Crete, Greece, 2019, pp. 24–26.

61. Ricci P, Verderame GM, Manfredi G. Analytical investigation of elastic period of infilled RC MRF buildings. Eng Struct. 2011;33:308–19. https://doi.org/10.1016/j.engstruct.2010.10.009.

62. De Risi MT, Del Gaudio C, Ricci P, Verderame GM. In-plane behaviour and damage assessment of masonry infills with hollow clay bricks in RC frames. Eng Struct. 2018;168:1. https://doi.org/10.1016/j.engstruct.2018.04.065.

63. Del Gaudio C, De Risi MT, Ricci P, Verderame GM. Empirical drift-fragility functions and loss estimation for infills in reinforced concrete frames under seismic loading. Bull Earthq Eng. 2019;17(3):1285–330. https://doi.org/10.1007/s10518-018-0501-y.

64. Al-Chaar GK. Evaluating strength and stiffness of unreinforced masonry infill structures. ERDC/CERL TR-02-1, 2002.

65. Fardis MN. Seismic design, assessment and retrofitting of concrete buildings: based on EN-Eurocode 8, Vol 8. Springer Science & Business Media, 2009.

66. Mainstone RJ. On the stiffnesses and strengths of infilled frames. Proc Inst Civ Eng. 1971;4:57–90.

67. Fardis MN. Experimental and numerical investigations on the seismic response of RC infilled frames and recommendations for code provisions. ECOEST/PREC8 Report No.6, Laboratorio Nacional de Engenharia Civil Publications, Lisbon, 1996.

68. Ricci P, Di Domenico M, Verderame GM. Out-of-plane seismic safety assessment of URM infills accounting for the in-plane/out-of-plane interaction in a nonlinear static framework. Eng Struct. 2019;195:96–112. https://doi.org/10.1016/j.engstruct.2019.05.088.

69. Calvi GM, Bolognini D. Seismic response of reinforced concrete frames infilled with weakly reinforced masonry panels. J Earthq Eng. 2001;5(2):153–85. https://doi.org/10.1080/13632460109350390.

70. Miano A, Mele A, Di Martire D, Infante D, Prota A, Ramondini M. Remote sensing data to support the structural monitoring of RC buildings affected by ground instability phenomena. In: Rivista Italiana di Geotecnica, N. 4/2021. ISSN: 0557-1405. 2021.

71. Ministerial Decree n. 24, 09/01/2020, Sisma Bonus-Linee guida per la classificazione del rischio sismico delle costruzioni nonché le modalità per l'attestazione, da parte di professionisti abilitati, dell'efficacia degli interventi effettuati, 2020 (in italian)

72. Di Lorenzo G, Colacurcio E, Di Filippo A, Formisano A, Massimilla A, Landolfo R. State-of-the-art on steel exoskeletons for seismic retrofit of existing RC buildings. Ingegneria Sismica. 2020;37(1):33–50.

73. Formisano A, Castaldo C, Chiumiento G. Optimal seismic upgrading of a reinforced concrete school building with metal-based devices using an efficient multi-criteria decision-making method. Struct Infrastruct Eng. 2017;13(11):1373–89. https://doi.org/10.1080/15732479.2016.1268174.

74. Formisano A, Sahoo DR. Steel shear panels as retrofitting system of existing multi-story RC buildings: Case studies. Adv Struct Eng Mech. 2015;1(495–512):2015. https://doi.org/10.1007/978-81-322-2190-6_41.

75. Moehle JP. State of research on seismic retrofit of concrete building structures in the US, US-Japan symposium and workshop on seismic retrofit of concrete structures, 2000.

76. Di Ludovico M, Balsamo A, Prota A, Manfredi G. Comparative assessment of seismic rehabilitation techniques on a full scale 3-story RC moment frame structure. Struct Eng Mech. 2008;28(6):727–48. https://doi.org/10.12989/sem.2008.28.6.727.

77. Thermou GE, Elnashai AS. Seismic retrofit schemes for RC structures and local-global consequences. Prog Struct Mat Eng. 2006;8(1):1–15. https://doi.org/10.1002/pse.208.